

EXTREME [OIII] EMITTERS AT $z \sim 0.5$

ZHIHUI LI^{1,2} AND MATTHEW A. MALKAN³

¹ Kavli Institute for Astronomy and Astrophysics, Peking University, Beijing 100871, China

² Department of Astronomy, School of Physics, Peking University, Beijing 100871, China

³ Physics and Astronomy Department, University of California, Los Angeles, CA 90095-1547

ABSTRACT

We have found a sample of extreme emission-line galaxies (EELGs) with very strong [OIII] λ 5007 emission at $z \sim 0.5$. Using broadband photometric selection, we searched the 14th Data Release (DR14) of the Sloan Digital Sky Survey (SDSS) and found 2658 candidates with strong i -band excess. We further obtained 649 spectra of these objects, and visually identified 22 [OIII] emitters lying at $0.40 < z < 0.63$. Having constructed their UV-IR spectral energy distributions (SED) we found that they have fairly blue r -W2 and red W1-W4 colors, indicative of strong warm dust emission. Their rest-frame [OIII] λ 5007 equivalent widths are mostly 200-600 Å and their high [OIII] λ 5007/H β ratios put them at the boundary of star-forming galaxies and AGNs on BPT diagrams. The typical $E(B - V)$ and electron temperature of [OIII] emitters is ~ 0.1 -0.3 mag and $\sim 10^4$ K, respectively. The lowest metallicity of our [OIII] emitters with $S/N_{[\text{OIII}]\lambda 4363} > 3$ is $12 + \log(\text{O}/\text{H}) = 7.99^{+0.22}_{-0.03}$, with a median value of $8.31^{+0.16}_{-0.08}$. Our [OIII] emitters exhibit remarkably high line luminosity – 18/22 have $L_{[\text{OIII}]\lambda 5007} > 5 \times 10^{42} \text{ erg s}^{-1}$ and 5/22 have $L_{[\text{OIII}]\lambda 5007} > 10^{43} \text{ erg s}^{-1}$. Their estimated volume number density at $z \sim 0.5$ is $\sim 3 \times 10^{-8} \text{ Mpc}^{-3}$, suggestive of a steep slope at the bright end of the [OIII] luminosity function.

Keywords: galaxies: dwarf — galaxies: emission lines — galaxies: evolution — galaxies: starburst

1. INTRODUCTION

Extreme emission-line galaxies (EELGs) are dwarf galaxies undergoing vigorous star formation characterized by very strong emission lines such as H α and [OIII]. Lying above the typical ‘galaxy main sequence’ (SFR- M_\star relation, Noeske et al. 2007), these relatively ‘primitive’ objects provide complementary opportunities for studying both the early epochs of star formation, and chemical evolution across cosmic history. Although EELGs are rare in the local universe (Cardamone et al. 2009), they could have been far more important, or even dominant, in the younger universe. To illustrate, recent slitless spectroscopy surveys (e.g. the WISP survey, Atek et al. 2010) in the near-infrared have shown that the number density of EELGs with high rest-frame EW > 200 Å could increase by a factor of ten or more at $z \sim 1.5$ (Atek et al. 2011, 2014); Malkan et al. (2017) concluded that even typical star-forming galaxies at $z \sim 3$ show extremely strong [OIII] emission lines with rest-frame equivalent widths (EW) of 500-900 Å. Moreover, the characteristic luminosity of EELGs (the ‘knee’ in their luminosity function, LF) also shifts to higher values at higher redshifts (Ly et al. 2007); the bright end of their LF is yet to be determined accurately.

A comprehensive survey of EELGs, which requires search-

ing over a very wide sky area with well-defined criteria, is observationally challenging. These objects are fairly compact and faint in all broad bands (such as the infrared (IR) or the X-rays). Their stellar populations are very young and blue and they do not exhibit obviously different optical colors from quasars. The largest population of EELGs discovered so far is by deep narrow-band filter imaging (Ly et al. 2007) but very large areas of sky have not yet been accessible to large-format cameras with such narrow-band imaging filters. This leaves us with the only practical method available — the combination of multiple broadband optical filter photometry.

In this work, we explore the properties of EELGs at $z \sim 0.5$, which are basically the counterparts of ‘Green Peas’ (Cardamone et al. 2009) at a higher redshift. It is worth noting the many additional advantages of increasing the sample of bright confirmed EELGs at $z \sim 0.5$. For example, our objects are particularly valuable for various follow-up observations, in that the brightest EELGs at this redshift can be spectroscopically observed in the rest-frame far-ultraviolet (UV), free from the absorption of intergalactic HI clouds. This may shed light on the Lyman leakage process, since we now have strong indications that the EELGs are the principal sources of ionizing photons (Yang et al. 2017a) that escaped into the intergalactic medium and re-ionized it at $z \sim 6$ or higher (Jaskot & Oey 2013).

This paper is organized as follows. In Section 2, we describe our photometric sample selection criteria quantitatively and present our results. We also discuss the contam-

^{1,2}zhihui.li.astro@gmail.com

³malkan@astro.ucla.edu

ination by other objects, such as $H\alpha$ emitters. In Section 3, we present spectra and SEDs of our [OIII] sample. We also derive an average spectrum for our [OIII] λ 5007 emitters. In Section 4 we explore both photometric and spectroscopic properties of our [OIII] λ 5007 emitters. We calculate the expected volume number density of [OIII] emitters at $z \sim 0.5$ in Section 4.9. In Section 5 we summarize our results. Throughout this paper we adopt a flat Λ CDM cosmology with $\Omega_m = 0.308$, $\Omega_\Lambda = 0.692$ and $H_0 = 67.8 \text{ km s}^{-1} \text{ Mpc}^{-1}$ (Planck Collaboration *et al.* 2016).

2. SAMPLE

2.1. Photometric Selection Criteria

Our parent sample is constructed from the *ugriz* photometry in PhotoPrimary catalog of the SDSS 14th Data Release (DR14, Abolfathi *et al.* 2017) using the CasJobs search tool¹. As the [OIII] λ 5007 line is shifted to *i*-band at $z \sim 0.5$, we expect our target EELGs to have strong *i*-band excess. The key selection criterion is:

$$i - z \leq r - i - 0.7 \quad (1)$$

which is essentially requiring an *i*-band excess compared to the *r* and *z* bands. We further require fairly blue colors for our objects, since starbursts have young stellar populations:

$$u - g \leq 0.3 \quad (2)$$

$$g - r \leq 0.45 \quad (3)$$

$$r - z \leq 0.8 \quad (4)$$

We also expect the *r* and *z* magnitudes of these compact and distant objects to be faint:

$$r, z \geq 18.5 \quad (5)$$

To ensure the high precision of our data, we also require a small uncertainty of our *u*-band, $\text{err}_u < 0.25$ (as *u*-band is usually the faintest among the five bands and carries relatively larger error bars) and $\text{err}_g, \text{err}_r, \text{err}_i, \text{err}_z < 0.15$. We use model magnitudes for all five bands. For more details, we refer readers to Appendix A, where the full SQL queries are presented.

As a result, we obtained 968 objects in total as our parent sample of [OIII] candidates with *i*-band excess. Next we searched for SDSS spectra of these objects in DR14. We found 200 observations, in which 75 objects are classified as ‘galaxy’ (based on image analysis) instead of ‘star’ or ‘QSO’ by the SDSS pipeline. With visual inspection of their spectra we identified 17 [OIII] λ 5007 emitters, whose redshifts lie in the range $0.40 < z < 0.63$. We have also tested searching in the PhotoObjectAll catalog (where multiple photometry of a certain object could exist) and it yielded a list of 2658 unique objects, of which 649 have observed SDSS spectra. In this sample we identified five more [OIII] emitters. However, this sample is less ‘clean’, in the sense that it is more

contaminated by local stars and QSOs. We refer to these two samples as the ‘primary sample’ and the ‘total sample’ respectively hereafter. For the sake of comprehensiveness, in the following analysis we study the 22 [OIII] emitters altogether.

The positions and *r*-band magnitudes of our ‘total sample’ are tabulated in Table 2. The distribution of the sizes (*r*-band Petrosian radius, *petrorad_r*) versus *r*-band magnitudes of 2658 [OIII] candidates is illustrated in Figure 2. The mean and median *petrorad_r* of our parent sample are 2.5 and 1.4 arcsec, respectively, and 95% of these [OIII] candidates have *petrorad_r* < 5 arcsec.

The effectiveness of our selection criteria is illustrated in Figure 1. We plotted colors of our 22 [OIII] emitters together with 10000 galaxies and 10000 QSOs. The galaxies and the QSOs are selected from DR14 and the SDSS 12th Data Release Quasar Catalog (DR12Q, Pâris *et al.* 2017) respectively by requiring that they have similar *r*-band magnitudes with [OIII] emitters ($19 < r < 21$). We use model magnitudes for galaxies and [OIII] emitters, and PSF magnitudes for QSOs. As can be seen in Figure 1, our candidates have successfully, if not perfectly, avoided the large populations of galaxies and QSOs.

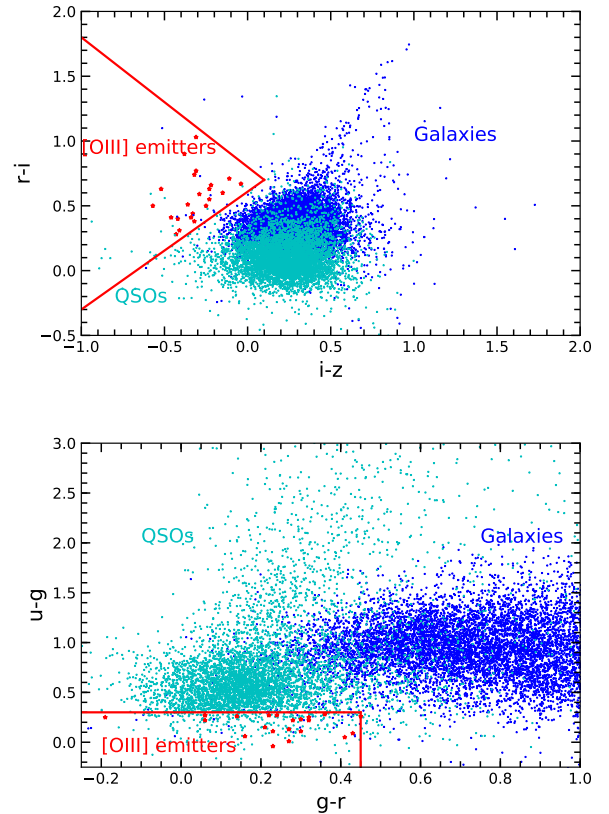
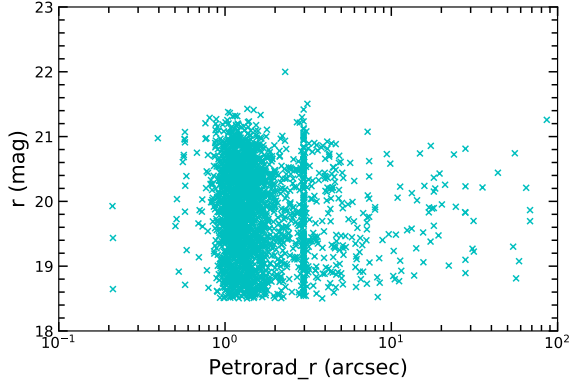
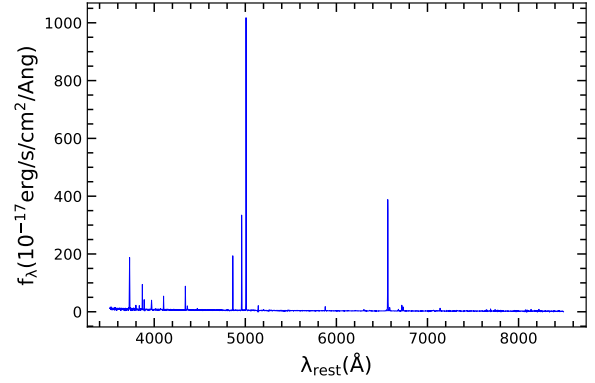


Figure 1. Color-color diagrams for 22 [OIII] emitters (red stars), a sample of normal galaxies (blue points) and a sample of QSOs (green points) with similar *r*-band magnitudes.

Table 1. Selection procedure used to construct our samples

Step	Selection Criteria	Number of Objects	
		Primary Sample	Total Sample
(1)	(2)	(3)	(4)
1	Eq. (1)-(5)	968	2658
2	Requiring SDSS spectra	200	649
3	Removing spectroscopically identified QSOs and stars	75	140
4	Picking [OIII] emitters by visual check on spectra	17	22

**Figure 2.** Distribution of the sizes (r -band Petrosian radius) v.s. r -band magnitude of 2658 [OIII] candidates.**Figure 3.** An example of rest-frame spectrum of a $H\alpha$ emitter (RA = 211.85546, Dec = 5.47718, $z = 0.085$). This spectrum is available in a machine-readable format online.**Table 2.** Positions and r -band magnitudes of our parent sample of 2658 [OIII] candidates

RA (J2000 deg)	Dec (J2000 deg)	r (mag)
(1)	(2)	(3)
0.06925	14.73523	19.70
0.11109	6.20795	19.60
0.11965	0.86930	18.78
0.30502	31.65254	19.90
0.46296	33.16742	20.01
0.51115	7.99360	21.15
1.01737	14.77081	19.84
1.33597	36.29656	20.95
1.48225	18.14386	18.97
1.48347	4.99813	20.18

Notes. Only the first ten columns are shown. Full version of this table is available in a machine-readable format online.

2.2. Contamination by $H\alpha$ Emitters, QSOs and stars

By examining the SDSS spectra of the objects in our sample, we find the contamination comes from mainly three types of objects: (a) $z \gtrsim 1$ QSOs; (b) $z \lesssim 0.2$ $H\alpha$ emitters; (c) local stars. The i -band excess of $z \gtrsim 1$ QSOs is caused by either the Mg II or the C III emission line. For the local stars, we examined all of them in our ‘primary sample’ (13 in total). We found two of them have [Ar III] emission that causes their i -band excess, while others’ photometry are unreliable and do not exhibit i -band excess in their spectra.

We also examined the composition of the 140 spectroscopically observed objects in our ‘total sample’, all of which are classified as ‘galaxies’ in SDSS DR14. When we require clean photometry (`clean=1`), most objects are excluded and only 22 identified [OIII] emitters and 22 $H\alpha$ emitters remained. The redshifts of these $H\alpha$ emitters range from 0.07 to 0.14, with a median value of 0.095, which accounts for their i -band excess. The rest-frame spectrum of one of these $H\alpha$ emitters is shown in Figure 3 as an example. We noticed that apart from strong $H\alpha$ emission, some of the $H\alpha$ emitters also exhibit comparably strong [OIII] λ 5007 emission to our [OIII] emitters. We will further compare the emission line properties of $H\alpha$ and [OIII] emitters in Section 4.

3. MULTI-WAVELENGTH OBSERVATIONS OF [OIII] EMITTERS

3.1. Photometry

¹ <https://skyserver.sdss.org/CasJobs>

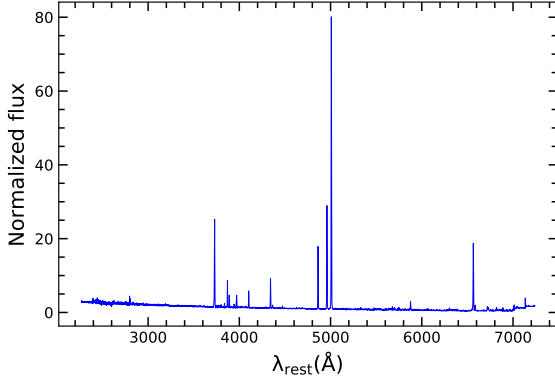


Figure 4. Average rest-frame spectra of 22 [OIII] emitters. This spectra is available in a machine-readable format online.

We have constructed UV-IR spectral energy distributions (SED) for each of our [OIII] emitters by collecting *GALEX*, SDSS, UKIDSS and WISE data from their corresponding online catalogs. For *GALEX* data, we searched for NUV and FUV detections using the *GALEX All-Sky Survey Source Catalog (GASC)* and *Medium Imaging Survey Catalog (GMSC)*². We reject data which have a Window or Dichroic flag. When multiple observations exist we select the deepest one, and when no detections are available we adopt the $3\text{-}\sigma$ upper limit. For SDSS data, we adopt the model magnitudes from DR14. To ensure all the magnitudes are on the AB system, we added -0.04 to measured u -band magnitudes and 0.02 to z -band magnitudes³.

For near-infrared data, we searched in **UKIDSS Large Area Survey (LAS)** from UKIDSSDR10PLUS database⁴ and chose the *aperMag6* magnitude, which corresponds to a ~ 5.6 arcsec diameter aperture. For WISE data, we collected *wxmp* profile-fit magnitudes from the **ALLWISE Source Catalog** (Cutri et al. 2013), as our [OIII] emitters are all identified as point sources (*ext_flg*=0). We further added small zero-point corrections of 0.03, 0.04, 0.03, -0.03 to W1-W4 magnitudes respectively following Jarrett et al. (2012). All SEDs for [OIII] emitters are presented in Appendix B.

3.2. Spectra

For our 22 [OIII] emitters, we have compiled their spectra and line measurements from SDSS. In Figure 4, we present the rest-frame mean spectra of our [OIII] emitters, which is the average of 22 normalized (using g -band continuum, 4500 Å) spectra. We also present the rest-frame spectrum of each [OIII] emitter in Appendix B. Strong [OIII] $\lambda 5007$ emission at $z \sim 0.5$ can be seen in each spectrum.

4. RESULTS

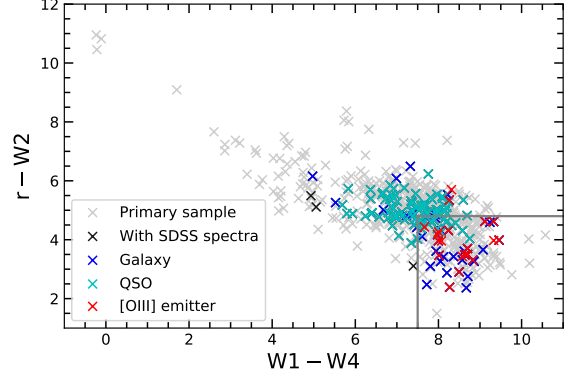


Figure 5. Distribution of $r\text{-}W2$ v.s. $W1\text{-}W4$ color for [OIII] emitters and our parent sample.

4.1. WISE Color

In addition to examining the effectiveness of our selection criteria by plotting color-color diagram of SDSS colors, we also studied the WISE colors. As illustrated in Figure 5, our [OIII] emitters have bluer $r\text{-}W2$ and redder $W1\text{-}W4$ colors compared to most other objects, especially quasars.

We further compare the WISE colors of our [OIII] emitters with 96 metal-deficient star-forming galaxies from Izotov et al. (2014). As the typical redshift of our [OIII] emitters is $z \sim 0.5$, we use NUV, i , W2, $(W2+W3)/2$, and W4 magnitudes that approximately cover the same rest-frame wavelengths as FUV, r , W1, W2 and W3 magnitudes of star-forming galaxies (mainly $z \lesssim 0.2$) in Izotov’s sample.

From Figure 6a, we can see that all of our [OIII] emitters detected in WISE have $W1\text{-}W2$ color redder than 1.6 mag. Such red $W1\text{-}W2$ colors are strongly indicative of hot dust emission of 400-600 K grains (Izotov et al. 2011). Moreover, our [OIII] emitters have redder $W1\text{-}W3$ and $W2\text{-}W3$ colors than Izotov’s sources, indicating that their strong $12\mu\text{m}$ emission is at or beyond the extreme seen in Izotov’s galaxies. The likely explanation is the extreme star formation in our sources.

From Figure 6b we can see that our [OIII] emitters have higher $W1\text{-}W3$ colors than Izotov’s sample, although the rest-frame $\text{EW}(\text{H}\beta)$ of both samples are similar. The lowest values of rest-frame $\text{EW}(\text{H}\beta)$ and $\text{H}\beta$ luminosity for our [OIII] emitters are 31 Å and $6.9 \times 10^{41}\text{ erg s}^{-1}$, respectively. The very intense burst of young star formation is evidently also effective in heating dust.

Figure 6c shows that our [OIII] emitters with high $\text{H}\beta$ luminosity and red $W1\text{-}W2$ colors have relatively high metallicity ($12 + \log(\text{O}/\text{H}) > 7.8$, calculated in Section 4.6). This might be because higher metallicity corresponds to larger amounts of dust, which emit more mid-infrared emission, heated in young star-forming regions.

4.2. EW of [OIII] $\lambda 5007$

We compiled the rest-frame EWs of [OIII] $\lambda 5007$ for both our [OIII] emitters and $\text{H}\alpha$ emitters. From Figure 7 we can see that the rest-frame EW of [OIII] emitters mainly range from 200 Å to 600 Å , which is also the case for $\text{H}\alpha$ emitters.

² <http://galex.stsci.edu/galexview/>

³ <http://www.sdss.org/dr14/algorithms/fluxcal/>

⁴ <http://wsa.roe.ac.uk/dbaccess.html>

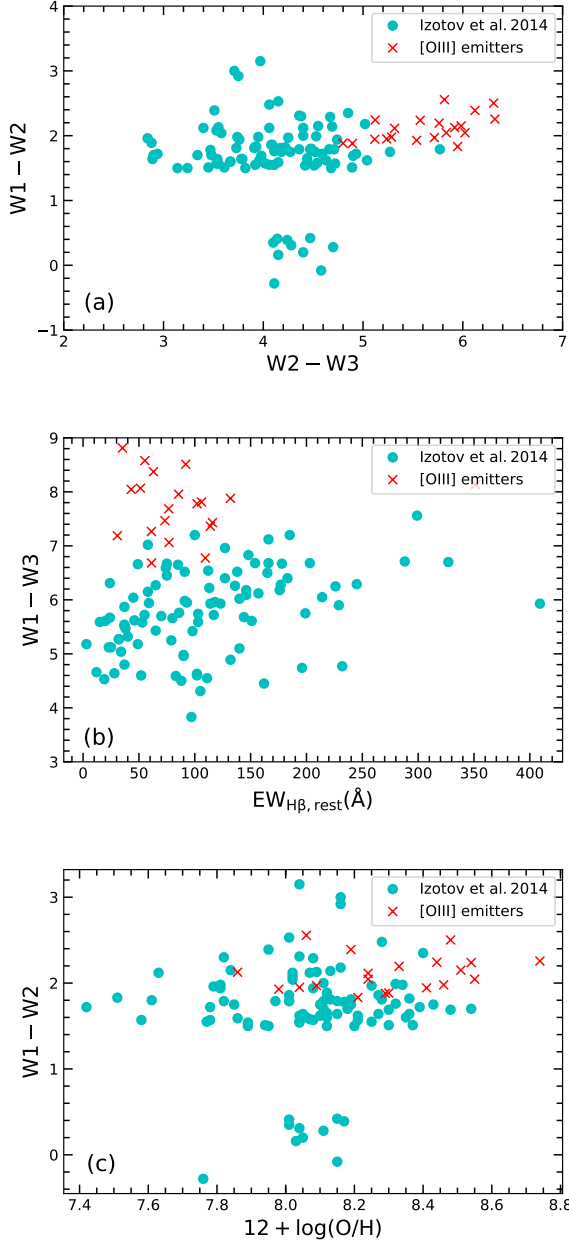


Figure 6. Comparison plots of WISE colors for [OIII] emitters and star-forming galaxies in Izotov et al. (2014). (a) W1-W2 v.s. W2-W3 color-color diagram. (b) W1-W3 v.s. $EW_{H\beta, \text{rest}}$ diagram. (c) W1-W2 v.s. $12 + \log(O/H)$ diagram. The metallicities of 22 [OIII] emitters are calculated in Section 4.6.

It is noteworthy that several $H\alpha$ emitters and [OIII] emitters exhibit extremely high rest-frame EW of $\sim 1000 \text{ \AA}$. Almost all [OIII] emitters have high $EW_{[OIII]\lambda 5007, \text{rest}}/EW_{H\beta, \text{rest}}$ ratios ($> 10^{0.5}$), indicative of the high ionization levels of their interstellar gas.

4.3. BPT Diagram

We used Baldwin-Phillips-Terlevich (BPT, hereafter) diagnostic line-ratio diagrams to infer the photoionization mechanisms in our [OIII] emitters. The most widely-used three BPT diagrams are relations of $[OIII]\lambda 5007/H\beta$ v.s.

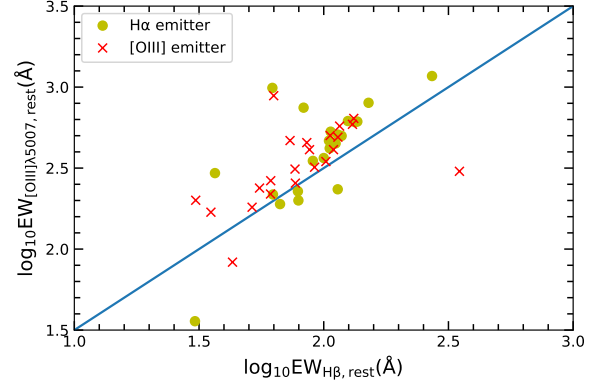


Figure 7. Comparison plot of rest-frame $EW_{[OIII]\lambda 5007}$ v.s. $EW_{H\beta}$ of [OIII] and $H\alpha$ emitters. The straight line is drawn from $EW_{[OIII]\lambda 5007, \text{rest}} = 10^{0.5} EW_{H\beta, \text{rest}}$.

$[NII]\lambda 6583/H\alpha$, $[SII]\lambda\lambda 6716, 6731/H\alpha$ and $[OI]\lambda 6300/H\alpha$. For the [NII]-BPT diagram (shown in Figure 8a), we included AGN/starburst boundary lines from Kauffmann et al. (2003) (shown in magenta) and Kewley et al. (2006) (shown in blue). For the [SII]-BPT and [OI]-BPT diagrams (shown in Figures 8b and 8c) we adopted the boundary lines from Kewley et al. (2006).

It can be seen from the BPT diagrams that our [OIII] emitters mainly lie just in the star-forming region, but near the AGN boundary. On the [NII]-BPT diagram, all [OIII] emitters with $H\alpha$ measurements lie in the HII region zone. On the [SII]-BPT and [OI]-BPT diagrams, we found three and five [OIII] emitters just across the boundary into Seyferts, respectively, while the rest lie with the HII regions. As a comparison, we also plotted the line ratios of the composite spectrum of 26 emission-line galaxies at $z \sim 2$ from Masters et al. (2014), which lie near our [OIII] emitters and the HII regions on the [NII]-BPT and [SII]-BPT diagrams.

4.4. Dust Extinction

We have estimated the amount of dust extinction from the observed Balmer decrements. Assuming the hydrogen nebular emission follows Case B recombination, the intrinsic Balmer flux ratios are $(H\alpha/H\beta)_0 = 2.86$, $(H\gamma/H\beta)_0 = 0.468$ and $(H\delta/H\beta)_0 = 0.259$ for $T_e = 10^4 \text{ K}$. We adopt the reddening curve of Cardelli et al. (1989), which gives

$$E(B - V) = 2.33 \log \left(\frac{H\alpha}{H\beta} \right)_{\text{obs}} - 1.06 \quad (6)$$

and

$$E(B - V) = -4.46 \log \left(\frac{H\gamma}{H\beta} \right)_{\text{obs}} - 1.47 \quad (7)$$

Since only 7/22 [OIII] emitters have $H\alpha$ line flux measurements, while all 22 emitters have $H\gamma$ line flux measurements, we calculated $E(B - V)$ in both ways using Equation (6) and (7) and present our results in Table 4. To estimate the uncertainties, we generated realizations of the emission line fluxes based on their S/N ratios, and constructed probability distri-

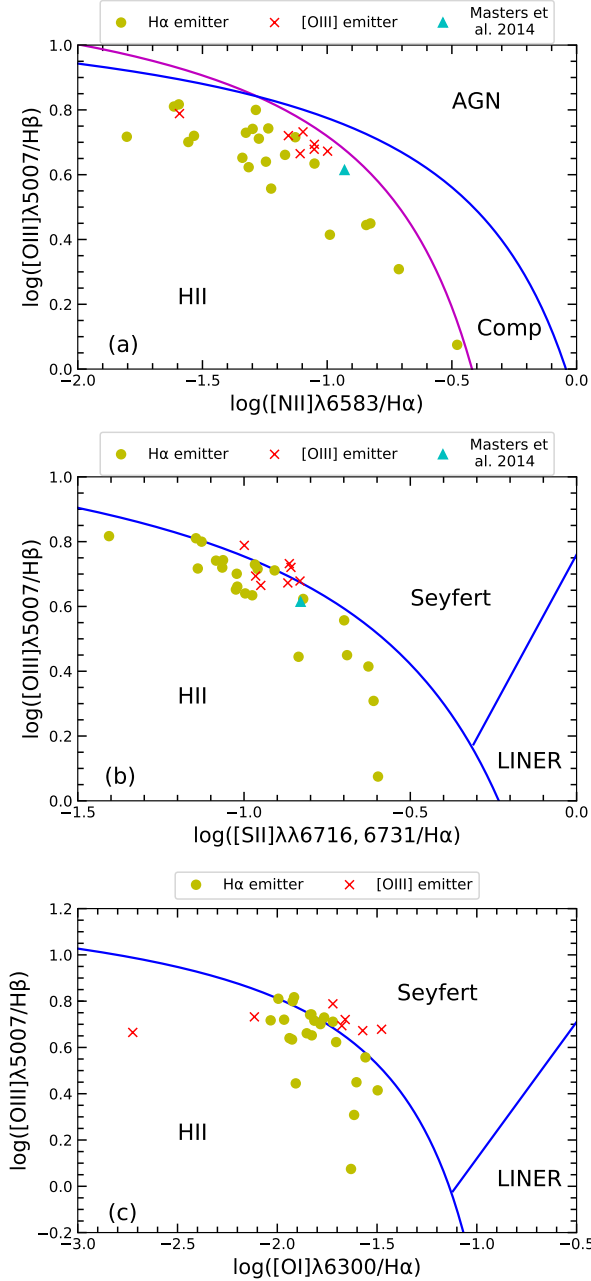


Figure 8. BPT diagrams of 22 [OIII] emitters and 22 H α emitters. ‘HII’ = normal star-forming galaxies. ‘Comp’ = composite galaxies. (a) The [NII]-BPT diagram, in which the AGN/starburst boundary lines are from Kauffmann et al. (2003) (shown in magenta) and Kewley et al. (2006) (shown in blue). (b)-(c) The [SII]-BPT and [OI]-BPT diagrams, in which the boundary lines are from Kewley et al. (2006), which separate normal star-forming galaxies from Seyferts and LINERs.

contributions of the emission line fluxes. The error bars given in Table 4 correspond to 68% confidence levels.

The typical value of $E(B - V)$ for our [OIII] emitters is ~ 0.1 - 0.3 mag. We found that although the extinction inferred from $H\gamma/H\beta$ ($E(B - V)_{H\gamma,H\beta}$) tends to be slightly higher than that from $H\alpha/H\beta$ ($E(B - V)_{H\alpha,H\beta}$), they are basically consistent considering their uncertainties. In the following calculations we adopted $E(B - V)_{H\alpha,H\beta}$ when they are available,

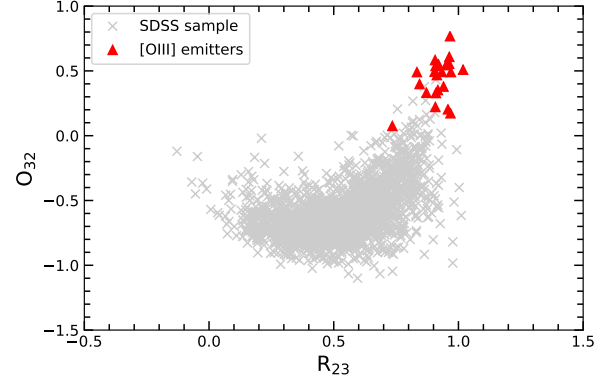


Figure 9. The distribution of O_{32} and R_{23} ratios of [OIII] emitters and the SDSS star-forming galaxies at $z \sim 0$. All ratios have been corrected for internal dust extinction.

and $E(B - V)_{H\gamma,H\beta}$ in other cases to correct for dust extinction (Section 4.6).

4.5. O_{32} and R_{23}

To better understand the ionization and excitation situation of our [OIII] emitters, we also calculated the O_{32} and R_{23} indices, defined as:

$$O_{32} = \log \frac{[\text{OIII}]\lambda\lambda 4959, 5007}{[\text{OII}]\lambda\lambda 3727, 3729} \quad (8)$$

$$R_{23} = \log \frac{[\text{OIII}]\lambda\lambda 4959, 5007 + [\text{OII}]\lambda\lambda 3727, 3729}{H\beta} \quad (9)$$

O_{32} and R_{23} are often used to independently characterize the degree of ionization in HII regions (Strom et al. 2017). Figure 9 shows the distribution of our [OIII] emitters on the O_{32} - R_{23} plane compared with $z \sim 0$ normal star-forming galaxies selected from the MPA-JHU⁵ catalog. This SDSS comparison sample is composed of 2000 $z < 0.1$ objects, classified as star-forming galaxies from BPT diagrams with a ‘reliable’ flag. All the O_{32} and R_{23} ratios have been corrected for internal dust extinction derived from Balmer decrements (see Eq. (6)).

As is shown in Figure 9, our [OIII] emitters mainly occupy the region with the highest O_{32} and R_{23} compared to the SDSS sample, indicative of the extreme high degrees of ionization of these objects. The maximum value of R_{23} for both samples is ~ 1 , as expected for star-forming galaxies with a maximum hardness of ionizing spectrum. Hard ionizing radiation fields and sub-solar oxygen abundances are required to reach the upper limit of R_{23} (Kewley & Dopita 2002; Lilly et al. 2003; Strom et al. 2017).

4.6. Electron Temperature and Metallicity

Following Ly et al. (2016a), we calculated electron temperatures (T_e) and gas-phase metallicities for our 22 [OIII]

⁵ http://www.sdss3.org/dr10/spectro/galaxy_mpajhu.php

emitters. T_e can be estimated from auroral-to-nebular [OIII] flux ratio R :

$$R \equiv \frac{F([\text{OIII}]\lambda 4363)}{F([\text{OIII}]\lambda 4959) + F([\text{OIII}]\lambda 5007)} \quad (10)$$

and

$$T_e = a(-\log(R) - b)^{-c} \quad (11)$$

where $a = 13205$, $b = 0.92506$, and $c = 0.98062$ (Nicholls et al. 2014). The typical value of our derived T_e is $\sim 10^4$ K. Correcting the nebular-to-auroral [OIII] flux ratio for internal dust extinction will slightly increase our estimates of T_e (~ 0.05 dex at most, see Table 6).

Next we determine the gas-phase ionic oxygen abundances using two emission-line flux ratios, [OII] $\lambda 3727/\text{H}\beta$ and [OIII] $\lambda\lambda 4959, 5007/\text{H}\beta$ (Izotov et al. 2006):

$$12 + \log\left(\frac{\text{O}^+}{\text{H}^+}\right) = \log\left(\frac{[\text{OII}]}{\text{H}\beta}\right) + 5.961 + \frac{1.676}{t_2} - 0.4\log t_2 - 0.034t_2 + \log(1 + 1.35x) \quad (12)$$

$$12 + \log\left(\frac{\text{O}^{++}}{\text{H}^+}\right) = \log\left(\frac{[\text{OIII}]}{\text{H}\beta}\right) + 6.200 + \frac{1.251}{t_3} - 0.55\log t_3 - 0.014t_3 \quad (13)$$

where $t_3 = T_e([\text{OIII}])/10^4$ K, $t_2 = T_e([\text{OII}])/10^4$ K and $x = 10^{-4}n_e t_3^{-0.5}$. We adopted $t_2 = 0.7t_3 + 0.17$ because $t_3 < 2.0$ is always true for our [OIII] emitters (Andrews & Martini 2013). For the electron density n_e , we assume $n_e = 100 \text{ cm}^{-3}$, but the results are almost independent of this assumption. The total oxygen abundance is given by $\text{O}/\text{H} = (\text{O}^+ + \text{O}^{++})/\text{H}^+$ since the most abundant ions of oxygen in HII regions are O^+ and O^{++} .

We also corrected $\frac{[\text{OIII}]\lambda\lambda 4959, 5007}{[\text{OIII}]\lambda 4363}$ and $\frac{[\text{OII}]\lambda 4363}{\text{H}\beta}$ for dust extinction and derived corresponding electron temperatures and metallicities. Both the dust-corrected and the dust-uncorrected results are shown in Table 6. For 15/22 [OIII] emitters with $\text{S/N} > 3$ detections of [OIII] $\lambda 4363$ (referred as '[OIII] $\lambda 4363$ -detected') we generated realizations of the emission line fluxes and constructed probability distributions. Their propagated error bars given in Table 6 correspond to 68% confidence levels. For the other 7/22 [OIII] emitters with $\text{S/N} < 3$ detections of [OIII] $\lambda 4363$ (referred as '[OIII] $\lambda 4363$ -non-detected') we calculated the upper limits of T_e and lower limits of metallicity.

As a result, for our [OIII] $\lambda 4363$ -detected sources, the lowest and median metallicities are $12 + \log(\text{O}/\text{H}) = 7.98^{+0.12}_{-0.02}$ and $8.24^{+0.05}_{-0.04}$. For our [OIII] $\lambda 4363$ -non-detected sources, the lowest and median metallicities are $12 + \log(\text{O}/\text{H}) = 7.86$ and 8.48 . Our results are comparable to the values from Ly et al. (2016b) (median $12 + \log(\text{O}/\text{H}) = 8.19^{+0.16}_{-0.19}$ for $0.3 < z \leq 0.5$, $\log M_\star = 9.25 \pm 0.25$ and $12 + \log(\text{O}/\text{H}) = 8.49^{+0.16}_{-0.00}$ for $0.5 < z \leq 1.0$, $\log M_\star = 10.00 \pm 0.25$).

4.7. Stellar Masses and Star Formation Rates

We estimate the stellar masses (M_\star) of our [OIII] emitters by performing UV-MIR SED fitting using CIGALE (Code

Investigating GALaxy Emission, Noll et al. 2009). The i -band photometry has been excluded from SED fitting as it contains strong [OIII] $\lambda 5007$ emission. We adopt a double-exponential star formation history model, composed of a main stellar population and a recent burst. The priors of the mass fraction and the age of the recent burst are set to be 0.01-0.99 and 10-100 Myr, respectively. We further incorporate BC03 (Bruzual & Charlot 2003) and DL07 (Draine & Li 2007) models to fit the stellar and dust emission. A Chabrier initial mass function (IMF) (Chabrier 2003) is assumed here, and the metallicities are fixed, using Eq. (18)-(20) from (Ly et al. 2016a). For internal dust extinction, we adopt a Calzetti et al. (2000) law with a free $E(B - V)$ varying from 0 to 2 mag. We also assume both the young and the old stellar population suffer from the same amount of extinction.

Our SED fitting results are summarized in Table 3. The derived stellar masses of our [OIII] emitters range from $10^{9.2} M_\odot$ to $10^{10.15} M_\odot$, with an average value of $10^{9.71} M_\odot$ and a median value of $10^{9.78} M_\odot$.

Next we derived the star formation rates (SFR) of our [OIII] emitters. We convert $\text{H}\alpha$ luminosity to SFR using the metallicity-dependent relation in Ly et al. (2016a). When $\text{H}\alpha$ is not measured we use $\text{H}\beta$ luminosity instead, assuming $(\text{H}\alpha/\text{H}\beta)_0 = 2.86$. The internal dust extinction has been corrected for all objects. The results are presented in Table 3. The SFR of our [OIII] emitters range from $10^{0.96} M_\odot \text{ yr}^{-1}$ to $10^{2.11} M_\odot \text{ yr}^{-1}$, with an average value of $10^{1.51} M_\odot \text{ yr}^{-1}$ and a median value of $10^{1.48} M_\odot \text{ yr}^{-1}$.

We then plot the SFR- M_\star and mass-metallicity relations for our [OIII] emitters. Compared with SFR- M_\star sequences in Peng et al. (2010) at $z \sim 0$ and Elbaz et al. (2007) at $z \sim 1$, our [OIII] emitters have much higher SFR, suggestive of vigorous recent starbursts. As for the mass-metallicity relation, after shifting the relations in Tremonti et al. (2004) at $z \sim 0.1$ and Savaglio et al. (2005) at $z \sim 0.7$ to Chabrier IMF, we found that our galaxies have fairly low metallicity compared to other star-forming galaxies.

Table 3. Stellar masses, SFRs and burst ages of 22 [OIII] emitters derived from SED fitting.

ID	$\log M_\star$ (M_\odot)	$\log \text{SFR}$ ($M_\odot \text{ yr}^{-1}$)	burst age (Myr)	$E(B - V)$ (mag)
(1)	(2)	(3)	(4)	(5)
OIII-1	$9.23^{+0.12}_{-0.16}$	$1.09^{+0.03}_{-0.04}$	71 ± 25	0.20 ± 0.01
OIII-2	$9.20^{+0.10}_{-0.13}$	$0.96^{+0.14}_{-0.10}$	55 ± 15	0.10 ± 0.01
OIII-3	$9.52^{+0.10}_{-0.13}$	$1.40^{+0.07}_{-0.12}$	98 ± 9	0.15 ± 0.05
OIII-4	$9.34^{+0.13}_{-0.18}$	$1.14^{+0.20}_{-0.03}$	67 ± 24	0.16 ± 0.05
OIII-5	$10.13^{+0.36}_{-\text{inf}}$	$1.09^{+0.04}_{-0.01}$	51 ± 6	0.22 ± 0.04
OIII-6	$10.15^{+0.08}_{-0.10}$	$2.06^{+0.28}_{-0.17}$	50 ± 4	0.30 ± 0.02
OIII-7	$9.52^{+0.29}_{-1.32}$	$1.44^{+0.02}_{-0.03}$	75 ± 25	0.17 ± 0.06
OIII-8	$9.48^{+0.09}_{-0.12}$	$1.50^{+0.02}_{-0.02}$	53 ± 13	0.20 ± 0.01
OIII-9	$9.81^{+0.10}_{-0.13}$	$1.50^{+0.01}_{-0.02}$	57 ± 18	0.29 ± 0.02
OIII-10	$9.89^{+0.10}_{-0.13}$	$1.53^{+0.00}_{-0.03}$	51 ± 7	0.20 ± 0.01
OIII-11	$9.45^{+0.12}_{-0.16}$	$1.46^{+0.01}_{-0.02}$	96 ± 14	0.10 ± 0.005
OIII-12	$9.52^{+0.11}_{-0.15}$	$1.44^{+0.20}_{-0.04}$	92 ± 18	0.10 ± 0.02

Table 3 continued

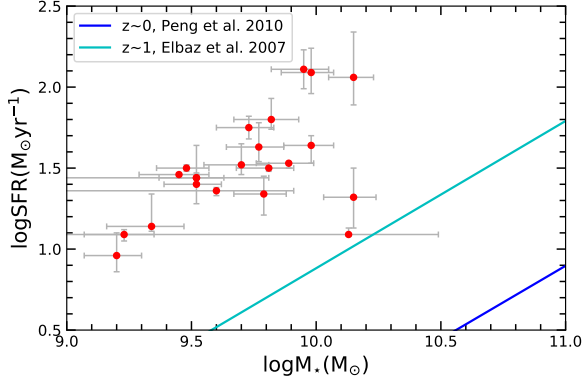


Figure 10. SFR v.s. stellar mass of 22 [OIII] emitters. Our results are shown in red solid circles. To compare our results with previous works, the sequences observed in Peng et al. (2010) at $z \sim 0$ and Elbaz et al. (2007) at $z \sim 1$ are shown in blue and cyan colors, respectively.

Table 3 (*continued*)

ID	$\log M_*$	$\log \text{SFR}$	burst age	$E(B - V)$
(1)	(2)	(3)	(4)	(5)
OIII-13	$9.77^{+0.10}_{-0.13}$	$1.63^{+0.15}_{-0.09}$	100 ± 5	0.11 ± 0.03
OIII-14	$9.70^{+0.11}_{-0.15}$	$1.52^{+0.13}_{-0.06}$	50 ± 3	0.29 ± 0.03
OIII-15	$9.60^{+0.31}_{-\text{inf}}$	$1.36^{+0.02}_{-0.03}$	78 ± 25	0.16 ± 0.06
OIII-16	$9.82^{+0.11}_{-0.15}$	$1.80^{+0.13}_{-0.06}$	80 ± 25	0.10 ± 0.005
OIII-17	$9.73^{+0.10}_{-0.13}$	$1.75^{+0.07}_{-0.07}$	86 ± 23	0.09 ± 0.02
OIII-18	$9.79^{+0.09}_{-0.12}$	$1.34^{+0.11}_{-0.13}$	50 ± 4	0.20 ± 0.01
OIII-19	$9.95^{+0.10}_{-0.13}$	$2.11^{+0.12}_{-0.12}$	98 ± 10	0.10 ± 0.005
OIII-20	$10.15^{+0.09}_{-0.12}$	$1.32^{+0.18}_{-0.19}$	104 ± 13	0.17 ± 0.05
OIII-21	$9.98^{+0.09}_{-0.12}$	$2.09^{+0.15}_{-0.13}$	51 ± 7	0.20 ± 0.01
OIII-22	$9.98^{+0.09}_{-0.11}$	$1.64^{+0.06}_{-0.11}$	100 ± 5	0.05 ± 0.01

Notes. Fitting results derived from CIGALE. (1) Object ID. (2) Stellar mass. (3) Star formation rate. (4) Age of the recent burst in Myr. (5) Color excess. Error bars correspond to 68% confidence levels.

4.8. UV Photometry v.s. Redshift

We calculated the ratios of NUV flux to FUV flux versus redshift (see Figure 12). A positive correlation between the $F_{\text{NUV}}/F_{\text{FUV}}$ ratio and redshift is observed, which we believe is the result of Lyman break absorption. All galaxies with $z > 0.55$ have a drop in FUV flux of at least a factor of ~ 3 compared to the NUV. This provides us with the possibility of predicting the redshift of [OIII] candidates, simply by calculating their $F_{\text{NUV}}/F_{\text{FUV}}$ ratio.

4.9. Line Luminosity and Number Density

We calculated the [OIII] $\lambda 5007$ line luminosity for our [OIII] emitters (provided in Table 5) from $L_{[\text{OIII}]\lambda 5007} = 4\pi d_L^2 F_{[\text{OIII}]\lambda 5007}$, where $F_{[\text{OIII}]\lambda 5007}$ is the [OIII] $\lambda 5007$ line flux and d_L is the luminosity distance. We found that our [OIII] emitters have remarkably high line luminosity:

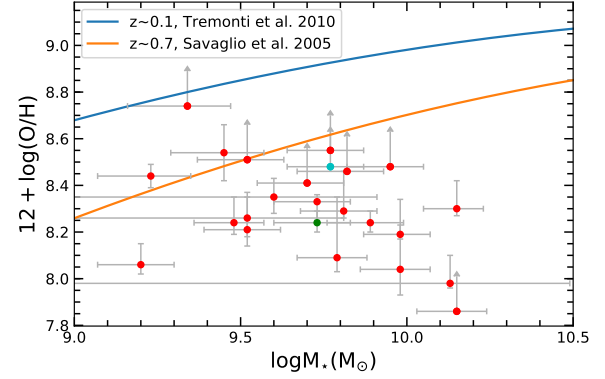


Figure 11. Metallicity v.s. stellar mass of 22 [OIII] emitters. Our results are shown in red solid circles. To compare our results with previous works, the fitting curves derived in Tremonti et al. (2004) at $z \sim 0.1$ and Savaglio et al. (2005) at $z \sim 0.7$ are shown in blue and orange colors, respectively. The green point is an artificial point with median metallicity and stellar mass of our [OIII] $\lambda 4363$ -detected sample. Similarly, the cyan point represents the median metallicity and stellar mass of our [OIII] $\lambda 4363$ -non-detected sample.

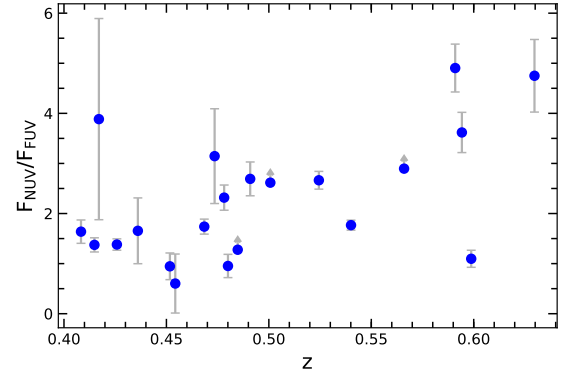


Figure 12. NUV to FUV ratio of 22 [OIII] emitters. The objects which only have 3- σ upper limits are marked with grey arrows.

18/22 have $L_{[\text{OIII}]\lambda 5007} > 5 \times 10^{42} \text{ erg s}^{-1}$ and 5 of them have $L_{[\text{OIII}]\lambda 5007} > 10^{43} \text{ erg s}^{-1}$. The mean and median $L_{[\text{OIII}]\lambda 5007}$ are $8.0 \times 10^{42} \text{ erg s}^{-1}$ and $7.9 \times 10^{42} \text{ erg s}^{-1}$, respectively.

We further estimated the expected volume number density of [OIII] emitters. First, we calculated the corresponding comoving volume searched by SDSS DR14 photometry:

$$\text{comoving volume} = \frac{\Omega}{4\pi} \frac{4\pi}{3} (R_{z_{\text{max}}}^3 - R_{z_{\text{min}}}^3) \quad (14)$$

where Ω is the sky coverage solid angle of SDSS DR14, $R_{z_{\text{max}}}$ and $R_{z_{\text{min}}}$ are the maximum and minimum comoving distance of our [OIII] emitters. With $\Omega = 14555 \text{ deg}^2$, $z_{\text{max}} = 0.630$ and $z_{\text{min}} = 0.415$ we derived a comoving volume = $1.288 \times 10^{10} \text{ Mpc}^3$.

Based on our photometric selection criteria, our search in the SDSS DR14 PhotoObjAll catalog derived 2658 unique objects, in which 514 are spectroscopically observed

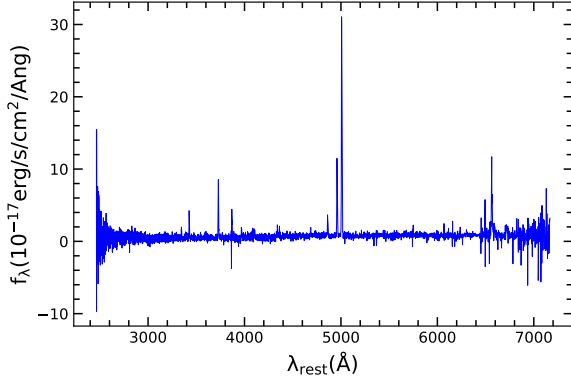


Figure 13. An example of rest-frame spectrum of a Seyfert 1.9 galaxy (RA = 190.40632, Dec = 10.95781, $z = 0.444$) misidentified as ‘starburst’ in SDSS. This spectrum is available in a machine-readable format online.

(some of them have more than one spectrum) and 22 are identified as [OIII] emitters at $z \sim 0.5$. To get a rough view of the total number of [OIII] emitters, we did another search in the SDSS DR14 `emissionLinesPort` catalog simply by requiring $EW_{[OIII]\lambda 5007} > 200 \text{ \AA}$ and $0.4 < z < 0.6$. In this way, we derived a sample of 981 objects with strong [OIII] emission. However, after checking their spectra we find only ~ 60 objects are real [OIII] starbursts (including all 22 [OIII] emitters except OIII-20) in this sample. Most objects are actually quasars or Seyfert 1.9 galaxies, because their spectra exhibit broad $H\alpha$ wings and [Ne V] lines (and some of them are misclassified as ‘starbursts’ by SDSS. A spectrum example is shown in Figure 13).

If we assume the fraction of [OIII] emitters is the same for those objects which have not yet been spectroscopically observed, we estimate the total number of [OIII] emitters should be ~ 350 in the corresponding comoving volume we searched photometrically. That means the number density of [OIII] emitters should be $\sim 3 \times 10^{-8} \text{ Mpc}^{-3}$. Here we compare our derived volume number density with previous works:

- (1) $\sim 3.0 \times 10^{-6} \text{ Mpc}^{-3}$ for EELGs at $z \lesssim 0.05$ (‘Blueberries’, Yang et al. 2017b);
- (2) $\sim 7.0 \times 10^{-6} \text{ Mpc}^{-3}$ for EELGs at $0.112 \lesssim z \lesssim 0.360$ (‘Green Peas’, Cardamone et al. 2009).

It can be seen that the number density of our [OIII] emitters is 100 to ~ 200 times lower than Blueberries and Green Peas. One possible explanation we propose here is their difference in line luminosity. Although the distribution of the rest-frame $EW_{[OIII]\lambda 5007}$, which range from 200 \AA to 600 \AA , and the brightness of continuum at corresponding wavelengths ($g/r/i$ -band, 18-20.5 mag) of our [OIII] emitters are similar to Blueberries and Green Peas, which indicates they have similar line flux $F_{[OIII]\lambda 5007}$, their line luminosity $L_{[OIII]\lambda 5007}$ differ a lot because of their different luminosity distances. In fact, the typical $L_{[OIII]\lambda 5007}$ for our [OIII] emitters, Green Peas and Blueberries are 10^{43} , 10^{42} and $10^{41} \text{ erg s}^{-1}$, respectively. Such high $L_{[OIII]\lambda 5007}$ could account for the scarcity of our [OIII] emitters.

Also, the decrease in number density (especially at $L_{[OIII]\lambda 5007} \sim 10^{42-43} \text{ erg s}^{-1}$) could be faster than previously thought (e.g. Ly et al. 2007), indicative of a steep slope at the bright end of the [OIII] LF. If we assume the volume density of [OIII] emitters at a certain $L_{[OIII]\lambda 5007}$, $\Phi(L)$, follows a power-law relation with respect to $L_{[OIII]\lambda 5007}$ (i.e. $\Phi(L) \propto L^{-\alpha}$), then the estimated α should be ~ 1 and ~ 2.5 , deducted by comparing our [OIII] emitters with Blueberries and Green Peas, respectively.

Table 4. Balmer decrements and derived extinction

ID (1)	$H\alpha/H\beta$ (2)	$H\gamma/H\beta$ (3)	$E(B-V)_{H\alpha, H\beta}$ (4)	$E(B-V)_{H\gamma, H\beta}$ (5)
OIII-1	...	$0.43^{+0.01}_{-0.00}$...	$0.15^{+0.03}_{-0.02}$
OIII-2	...	$0.45^{+0.02}_{-0.02}$...	$0.09^{+0.08}_{-0.09}$
OIII-3	...	$0.44^{+0.02}_{-0.01}$...	$0.13^{+0.06}_{-0.07}$
OIII-4	...	$0.45^{+0.02}_{-0.02}$...	$0.09^{+0.08}_{-0.09}$
OIII-5	$3.61^{+0.10}_{-0.11}$	$0.39^{+0.03}_{-0.01}$	$0.22^{+0.04}_{-0.01}$	$0.29^{+0.07}_{-0.11}$
OIII-6	...	$0.37^{+0.03}_{-0.03}$...	$0.44^{+0.15}_{-0.17}$
OIII-7	$3.68^{+0.12}_{-0.06}$	$0.35^{+0.02}_{-0.00}$	$0.28^{+0.01}_{-0.04}$	$0.51^{+0.07}_{-0.06}$
OIII-8	$3.66^{+0.07}_{-0.06}$	$0.39^{+0.01}_{-0.01}$	$0.24^{+0.03}_{-0.01}$	$0.36^{+0.06}_{-0.05}$
OIII-9	$3.46^{+0.12}_{-0.01}$	$0.40^{+0.01}_{-0.02}$	$0.21^{+0.02}_{-0.01}$	$0.30^{+0.08}_{-0.03}$
OIII-10	$3.34^{+0.09}_{-0.04}$	$0.44^{+0.01}_{-0.01}$	$0.16^{+0.02}_{-0.02}$	$0.12^{+0.03}_{-0.05}$
OIII-11	$3.18^{+0.02}_{-0.12}$	$0.43^{+0.01}_{-0.01}$	$0.10^{+0.01}_{-0.03}$	$0.15^{+0.09}_{-0.01}$
OIII-12	...	$0.41^{+0.02}_{-0.01}$...	$0.26^{+0.07}_{-0.09}$
OIII-13	...	$0.38^{+0.02}_{-0.02}$...	$0.35^{+0.12}_{-0.05}$
OIII-14	...	$0.40^{+0.01}_{-0.01}$...	$0.30^{+0.05}_{-0.08}$
OIII-15	$3.05^{+0.05}_{-0.08}$	$0.42^{+0.01}_{-0.01}$	$0.06^{+0.03}_{-0.02}$	$0.19^{+0.06}_{-0.03}$
OIII-16	...	$0.41^{+0.01}_{-0.01}$...	$0.27^{+0.07}_{-0.06}$

Table 4 continued

Table 4 (*continued*)

ID	H α /H β	H γ /H β	$E(B - V)_{\text{H}\alpha, \text{H}\beta}$	$E(B - V)_{\text{H}\gamma, \text{H}\beta}$
(1)	(2)	(3)	(4)	(5)
OIII-17	...	$0.42^{+0.02}_{-0.00}$...	$0.18^{+0.06}_{-0.04}$
OIII-18	...	$0.45^{+0.02}_{-0.01}$...	$0.09^{+0.06}_{-0.10}$
OIII-19	...	$0.34^{+0.02}_{-0.00}$...	$0.55^{+0.11}_{-0.05}$
OIII-20	...	$0.40^{+0.03}_{-0.02}$...	$0.20^{+0.19}_{-0.07}$
OIII-21	...	$0.33^{+0.02}_{-0.02}$...	$0.61^{+0.15}_{-0.06}$
OIII-22	...	$0.43^{+0.01}_{-0.02}$...	$0.13^{+0.12}_{-0.01}$

Notes. (1) Object ID. (2) Flux ratio of H α and H β . (3) Flux ratio of H γ and H β . (4) Color excess derived from H α /H β . (5) Color excess derived from H γ /H β . The uncertainties correspond to 68% confidence levels.

Table 5. Emission line properties of 22 [OIII] λ 5007 emitters

ID	RA	Dec	z	$\log\left(\frac{[\text{NII}]}{\text{H}\alpha}\right)$	$\log\left(\frac{[\text{SII}]}{\text{H}\alpha}\right)$	$\log\left(\frac{[\text{OI}]}{\text{H}\alpha}\right)$	EW _{[OIII]λ5007, obs}	F _{[OIII]λ5007}	L _{[OIII]λ5007}
	(J2000 deg)	(J2000 deg)					(\AA)	($10^{-17} \text{erg s}^{-1} \text{cm}^{-2}$)	(erg s^{-1})
(1)	(2)	(3)	(4)	(5)	(6)	(7)	(8)	(9)	(10)
OIII-1	124.27618	31.98355	0.408	691	626	3.9×10^{42}
OIII-2	28.87035	-1.12973	0.415	1252	781	5.1×10^{42}
OIII-3	237.06111	7.45281	0.417	492	1221	8.1×10^{42}
OIII-4	1.92919	0.04127	0.426	339	507	3.5×10^{42}
OIII-5	144.25380	36.43289	0.436	-1.59 ± 0.07	-1.00 ± 0.03	-1.72 ± 0.08	672	619	4.5×10^{42}
OIII-6	238.81838	35.72351	0.452	384	1695	1.4×10^{43}
OIII-7	182.09547	15.40173	0.454	-1.05 ± 0.02	-0.83 ± 0.03	-1.48 ± 0.03	597	694	5.6×10^{42}
OIII-8	153.74986	3.16105	0.468	-1.05 ± 0.02	-0.97 ± 0.03	-1.68 ± 0.04	941	860	7.5×10^{42}
OIII-9	142.94537	60.62296	0.474	-1.00 ± 0.03	-0.87 ± 0.03	-1.57 ± 0.04	606	857	7.7×10^{42}
OIII-10	135.89416	17.78826	0.478	-1.10 ± 0.02	-0.86 ± 0.02	-2.1 ± 0.9	849	1224	1.1×10^{43}
OIII-11	244.89253	22.32658	0.480	-1.11 ± 0.03	-0.95 ± 0.08	< -2.7	743	906	8.4×10^{42}
OIII-12	48.98032	-1.07757	0.485	450	531	5.0×10^{42}
OIII-13	16.18940	0.22369	0.491	269	564	5.5×10^{42}
OIII-14	211.53847	49.04090	0.501	383	500	5.1×10^{42}
OIII-15	350.74701	23.02511	0.507	-1.16 ± 0.05	-0.86 ± 0.10	-1.66 ± 0.07	888	927	9.8×10^{42}
OIII-16	25.73972	1.14013	0.524	333	890	1.0×10^{43}
OIII-17	31.94996	0.79318	0.540	700	1413	1.7×10^{43}
OIII-18	27.44835	1.00270	0.566	488	670	9.2×10^{42}
OIII-19	132.92699	50.61637	0.591	269	540	8.2×10^{42}
OIII-20	3.57051	0.23331	0.594	132	210	3.2×10^{42}
OIII-21	244.17766	20.95559	0.599	320	569	9.0×10^{42}
OIII-22	49.99925	-1.08055	0.630	522	850	1.5×10^{43}

Notes. (2)-(3) Right ascension and declination. (4) Redshift. (5)-(7) Emission line ratios of [NII]/H α , [SII]/H α and [OI]/H α . (8) Observed-frame equivalent width of [OIII] λ 5007. (9) Emission line flux of [OIII] λ 5007. (10) Line luminosity of [OIII] λ 5007. Column (8) and (9) are taken from the default emission line fits in SDSS DR14. The uncertainties correspond to 68% confidence levels.

Table 6. Emission-line ratios, electron temperatures and metallicities

ID	$\log\left(\frac{[\text{OIII}]\lambda\lambda 4959,5007}{[\text{OIII}]\lambda 4363}\right)$		$\log(\text{T}_\text{e}/\text{K})$		$\log\left(\frac{[\text{OII}]}{\text{H}\beta}\right)$		$\log\left(\frac{[\text{OIII}]}{\text{H}\beta}\right)$	$\log\left(\frac{\text{O}^+}{\text{H}^+}\right)$		$\log\left(\frac{\text{O}^{++}}{\text{H}^+}\right)$		$12 + \log\left(\frac{\text{O}}{\text{H}}\right)$	
(1)	(2)	(3)	(4)	(5)	(6)	(7)	(8)	(9)	(10)	(11)	(12)	(13)	(14)
OIII-1	$2.28^{+0.07}_{-0.03}$	$2.25^{+0.06}_{-0.03}$	$3.99^{+0.01}_{-0.02}$	$4.00^{+0.01}_{-0.02}$	$-0.17^{+0.01}_{-0.00}$	$-0.10^{+0.01}_{-0.00}$	$0.87^{+0.00}_{-0.00}$	$-4.17^{+0.01}_{-0.11}$	$-4.22^{+0.08}_{-0.04}$	$-3.68^{+0.10}_{-0.00}$	$-3.71^{+0.08}_{-0.02}$	$8.41^{+0.11}_{-0.00}$	$8.44^{+0.05}_{-0.05}$

Table 6 continued

Table 6 (continued)

ID	$\log\left(\frac{[\text{OIII}]\lambda\lambda 4959,5007}{[\text{OIII}]\lambda 4363}\right)$	$\log(\text{Te/K})$	$\log\left(\frac{[\text{OII}]}{\text{H}\beta}\right)$	$\log\left(\frac{[\text{OIII}]}{\text{H}\beta}\right)$	$\log\left(\frac{\text{O}^+}{\text{H}^+}\right)$	$\log\left(\frac{\text{O}^{++}}{\text{H}^+}\right)$	$12 + \log\left(\frac{\text{O}}{\text{H}}\right)$						
(1)	(2)	(3)	(4)	(5)	(6)	(7)	(8)	(9)	(10)	(11)	(12)	(13)	(14)
OIII-2	$1.99^{+0.06}_{-0.05}$	$1.96^{+0.06}_{-0.05}$	$4.08^{+0.03}_{-0.01}$	$4.10^{+0.02}_{-0.02}$	$-0.26^{+0.01}_{-0.03}$	$-0.23^{+0.03}_{-0.02}$	$0.90^{+0.02}_{-0.01}$	$-4.78^{+0.13}_{-0.03}$	$-4.74^{+0.10}_{-0.06}$	$-3.95^{+0.05}_{-0.08}$	$-4.01^{+0.09}_{-0.04}$	$8.06^{+0.11}_{-0.02}$	$8.06^{+0.09}_{-0.04}$
OIII-3	$2.12^{+0.15}_{-0.03}$	$2.07^{+0.16}_{-0.02}$	$4.04^{+0.02}_{-0.04}$	$4.04^{+0.03}_{-0.03}$	$-0.18^{+0.03}_{-0.01}$	$-0.11^{+0.01}_{-0.02}$	$0.81^{+0.00}_{-0.01}$	$-4.48^{+0.23}_{-0.02}$	$-4.31^{+0.07}_{-0.17}$	$-3.82^{+0.09}_{-0.12}$	$-3.88^{+0.09}_{-0.11}$	$8.22^{+0.16}_{-0.06}$	$8.21^{+0.14}_{-0.07}$
OIII-4	>2.65	>2.63	<3.89	<3.89	$-0.13^{+0.02}_{-0.02}$	$-0.08^{+0.02}_{-0.02}$	$0.71^{+0.01}_{-0.00}$	>3.76	>3.75	>3.42	>3.44	>8.74	>8.74
OIII-5	$1.95^{+0.05}_{-0.06}$	$1.84^{+0.08}_{-0.03}$	$4.11^{+0.02}_{-0.02}$	$4.16^{+0.01}_{-0.04}$	$-0.08^{+0.01}_{-0.01}$	$+0.06^{+0.01}_{-0.02}$	$0.91^{+0.01}_{-0.01}$	$-4.64^{+0.12}_{-0.04}$	$-4.60^{+0.10}_{-0.07}$	$-3.99^{+0.05}_{-0.08}$	$-4.14^{+0.12}_{-0.02}$	$8.03^{+0.13}_{-0.01}$	$7.98^{+0.12}_{-0.02}$
OIII-6	$2.32^{+0.07}_{-0.07}$	$2.20^{+0.06}_{-0.06}$	$3.98^{+0.02}_{-0.02}$	$4.02^{+0.02}_{-0.02}$	$-0.12^{+0.01}_{-0.00}$	$+0.09^{+0.01}_{-0.01}$	$0.77^{+0.00}_{-0.01}$	$-4.16^{+0.10}_{-0.07}$	$-4.12^{+0.11}_{-0.05}$	$-3.72^{+0.06}_{-0.08}$	$-3.90^{+0.11}_{-0.03}$	$8.41^{+0.08}_{-0.07}$	$8.30^{+0.12}_{-0.03}$
OIII-7	$2.22^{+0.10}_{-0.06}$	$2.10^{+0.07}_{-0.08}$	$4.01^{+0.02}_{-0.03}$	$4.05^{+0.03}_{-0.03}$	$-0.07^{+0.01}_{-0.01}$	$+0.17^{+0.01}_{-0.02}$	$0.80^{+0.01}_{-0.01}$	$-4.25^{+0.15}_{-0.06}$	$-4.07^{+0.03}_{-0.18}$	$-3.82^{+0.13}_{-0.05}$	$-3.92^{+0.07}_{-0.10}$	$8.32^{+0.13}_{-0.06}$	$8.26^{+0.11}_{-0.08}$
OIII-8	$2.22^{+0.10}_{-0.04}$	$2.11^{+0.11}_{-0.03}$	$4.00^{+0.02}_{-0.02}$	$4.05^{+0.01}_{-0.04}$	$-0.25^{+0.03}_{-0.00}$	$-0.08^{+0.03}_{-0.00}$	$0.82^{+0.01}_{-0.01}$	$-4.37^{+0.10}_{-0.07}$	$-4.36^{+0.15}_{-0.04}$	$-3.78^{+0.10}_{-0.05}$	$-3.88^{+0.10}_{-0.06}$	$8.34^{+0.08}_{-0.07}$	$8.24^{+0.11}_{-0.05}$
OIII-9	$2.31^{+0.08}_{-0.10}$	$2.15^{+0.16}_{-0.01}$	$3.98^{+0.03}_{-0.03}$	$4.00^{+0.03}_{-0.02}$	$-0.13^{+0.01}_{-0.01}$	$+0.06^{+0.01}_{-0.01}$	$0.79^{+0.01}_{-0.00}$	$-4.11^{+0.04}_{-0.19}$	$-4.22^{+0.18}_{-0.03}$	$-3.78^{+0.18}_{-0.03}$	$-3.89^{+0.18}_{-0.00}$	$8.38^{+0.15}_{-0.06}$	$8.29^{+0.17}_{-0.03}$
OIII-10	$2.12^{+0.03}_{-0.03}$	$2.06^{+0.06}_{-0.01}$	$4.04^{+0.01}_{-0.01}$	$4.06^{+0.01}_{-0.01}$	$-0.02^{+0.01}_{-0.01}$	$+0.04^{+0.01}_{-0.01}$	$0.85^{+0.01}_{-0.00}$	$-4.31^{+0.05}_{-0.04}$	$-4.30^{+0.05}_{-0.04}$	$-3.87^{+0.04}_{-0.03}$	$-3.90^{+0.04}_{-0.04}$	$8.25^{+0.06}_{-0.02}$	$8.24^{+0.05}_{-0.04}$
OIII-11	$2.43^{+0.11}_{-0.10}$	$2.33^{+0.14}_{-0.06}$	$3.95^{+0.03}_{-0.03}$	$3.97^{+0.02}_{-0.04}$	$-0.07^{+0.02}_{-0.01}$	$+0.04^{+0.01}_{-0.01}$	$0.79^{+0.00}_{-0.01}$	$-3.97^{+0.14}_{-0.11}$	$-4.01^{+0.20}_{-0.05}$	$-3.65^{+0.19}_{-0.03}$	$-3.72^{+0.19}_{-0.04}$	$8.53^{+0.16}_{-0.07}$	$8.54^{+0.12}_{-0.12}$
OIII-12	>2.45	>2.38	<3.94	<3.96	$-0.07^{+0.01}_{-0.02}$	$+0.05^{+0.01}_{-0.02}$	$0.72^{+0.01}_{-0.01}$	>3.94	>3.90	>3.63	>3.70	>8.54	>8.51
OIII-13	>2.46	>2.36	<3.94	<3.97	$-0.05^{+0.03}_{-0.00}$	$+0.12^{+0.01}_{-0.02}$	$0.78^{+0.01}_{-0.01}$	>3.91	>3.85	>3.56	>3.67	>8.60	>8.55
OIII-14	>2.34	>2.26	<3.97	<4.00	$-0.00^{+0.02}_{-0.01}$	$+0.15^{+0.01}_{-0.02}$	$0.71^{+0.02}_{-0.00}$	>4.01	>3.96	>3.76	>3.83	>8.44	>8.41
OIII-15	$2.25^{+0.05}_{-0.07}$	$2.14^{+0.12}_{-0.01}$	$4.00^{+0.02}_{-0.02}$	$4.02^{+0.02}_{-0.02}$	$-0.08^{+0.01}_{-0.01}$	$+0.02^{+0.01}_{-0.01}$	$0.84^{+0.01}_{-0.00}$	$-4.24^{+0.12}_{-0.04}$	$-4.19^{+0.09}_{-0.07}$	$-3.71^{+0.05}_{-0.09}$	$-3.80^{+0.08}_{-0.06}$	$8.36^{+0.11}_{-0.04}$	$8.35^{+0.08}_{-0.07}$
OIII-16	>2.44	>2.36	<3.94	<3.97	$-0.15^{+0.02}_{-0.02}$	$-0.03^{+0.03}_{-0.01}$	$0.71^{+0.01}_{-0.00}$	>4.03	>4.00	>3.65	>3.73	>8.50	>8.46
OIII-17	$2.16^{+0.09}_{-0.02}$	$2.12^{+0.07}_{-0.03}$	$4.02^{+0.02}_{-0.02}$	$4.06^{+0.00}_{-0.04}$	$-0.09^{+0.01}_{-0.02}$	$-0.01^{+0.02}_{-0.01}$	$0.86^{+0.01}_{-0.01}$	$-4.32^{+0.11}_{-0.04}$	$-4.33^{+0.14}_{-0.00}$	$-3.78^{+0.07}_{-0.05}$	$-3.85^{+0.09}_{-0.03}$	$8.32^{+0.09}_{-0.03}$	$8.33^{+0.03}_{-0.08}$
OIII-18	$2.00^{+0.24}_{-0.03}$	$2.04^{+0.17}_{-0.09}$	$4.09^{+0.01}_{-0.08}$	$4.07^{+0.04}_{-0.06}$	$-0.11^{+0.03}_{-0.02}$	$-0.06^{+0.02}_{-0.02}$	$0.83^{+0.01}_{-0.02}$	$-4.56^{+0.32}_{-0.04}$	$-4.46^{+0.23}_{-0.13}$	$-3.97^{+0.21}_{-0.10}$	$-4.00^{+0.21}_{-0.09}$	$8.11^{+0.25}_{-0.07}$	$8.09^{+0.26}_{-0.06}$
OIII-19	>2.41	>2.27	<3.95	<3.99	$-0.03^{+0.01}_{-0.02}$	$+0.23^{+0.01}_{-0.01}$	$0.77^{+0.01}_{-0.01}$	>3.94	>3.86	>3.62	>3.78	>8.55	>8.48
OIII-20	>2.01	>1.96	<4.09	<4.11	$-0.06^{+0.05}_{-0.00}$	$+0.06^{+0.03}_{-0.02}$	$0.47^{+0.03}_{-0.01}$	>4.50	>4.46	>4.37	>4.42	>7.87	>7.86
OIII-21	$1.87^{+0.20}_{-0.03}$	$2.01^{+0.28}_{-0.12}$	$4.14^{+0.01}_{-0.08}$	$4.02^{+0.11}_{-0.04}$	$-0.12^{+0.03}_{-0.02}$	$+0.18^{+0.01}_{-0.04}$	$0.78^{+0.01}_{-0.01}$	$-4.53^{+0.29}_{-0.03}$	$-4.38^{+0.20}_{-0.14}$	$-3.96^{+0.16}_{-0.11}$	$-4.21^{+0.22}_{-0.06}$	$8.09^{+0.24}_{-0.04}$	$8.04^{+0.19}_{-0.11}$
OIII-22	$2.14^{+0.10}_{-0.05}$	$2.07^{+0.12}_{-0.02}$	$4.03^{+0.02}_{-0.03}$	$4.04^{+0.03}_{-0.03}$	$-0.09^{+0.02}_{-0.01}$	$-0.04^{+0.03}_{-0.00}$	$0.83^{+0.01}_{-0.01}$	$-4.34^{+0.12}_{-0.07}$	$-4.29^{+0.08}_{-0.11}$	$-3.87^{+0.11}_{-0.06}$	$-3.90^{+0.09}_{-0.07}$	$8.26^{+0.11}_{-0.06}$	$8.19^{+0.15}_{-0.02}$

Notes. (2)-(3) Flux ratio of [OIII] $\lambda\lambda 4959, 5007$ to [OIII] $\lambda 4363$. (4)-(5) Electron temperature. (6)-(7) Flux ratio of [OII] $\lambda 3727$ to H β . (8) Flux ratio of [OIII] $\lambda\lambda 4959, 5007$ to H β . (9)-(10) Gas-phase abundance of O^+/H^+ . (11) Gas-phase abundance of O^+/H^+ . (12)-(13) Gas-phase abundance of oxygen. Columns (3), (5), (7), (10) and (13) have been corrected for internal dust extinction using Cardelli et al. (1989) law.

5. SUMMARY

We have searched for [OIII] emitters at $z \sim 0.5$ from SDSS broadband photometry, and confirmed a subset of them with SDSS spectroscopy. Our main results are as follows:

(1) We have established a simple way to select EELGs with i -band excess based on broadband photometry. Our selection criteria not only provide us with 22 spectroscopically confirmed [OIII] emitters at $z \sim 0.5$, but also offer a list of 2658 [OIII] candidates;

(2) Our [OIII] emitters have fairly blue r -W2 and red W1-W4 colors, compared to most other objects that also satisfy our selection criteria. All of our [OIII] emitters have W1-W2 ≥ 1.6 mag, strongly indicative of warm dust emission of 400-600 K. Their strong H β emission implies that they have very young star-forming regions, which could serve as the heating source of dust;

(3) The rest-frame [OIII] $\lambda 5007$ equivalent widths of our [OIII] emitters mainly range from 200 Å to 600 Å and their high [OIII] $\lambda 5007/\text{H}\beta$ ratios put them at the boundary of star-forming galaxies and AGNs on BPT diagrams;

(4) The typical $E(B-V)$ and electron temperature of [OIII] emitters is ~ 0.1 -0.3 mag and $\sim 10^4$ K, respectively;

(5) For our [OIII] $\lambda 4363$ -detected sources, the lowest and median metallicities are $12 + \log(\text{O}/\text{H}) = 7.98^{+0.12}_{-0.02}$ and $8.24^{+0.05}_{-0.04}$. For our [OIII] $\lambda 4363$ non-detected sources, the

lowest and median metallicities are $12 + \log(\text{O}/\text{H}) = 7.86$ and 8.48. Our results are comparable to the values in Ly et al. (2016b);

(6) By performing SED fitting using CIGALE, we derived stellar masses of our [OIII] emitters, which range from $10^{9.2} M_\odot$ to $10^{10.15} M_\odot$, with an average value of $10^{9.71} M_\odot$ and a median value of $10^{9.78} M_\odot$. By converting H α luminosity to SFR, we derived SFR of our [OIII] emitters, which range from $10^{0.96} M_\odot \text{ yr}^{-1}$ to $10^{2.11} M_\odot \text{ yr}^{-1}$, with an average value of $10^{1.51} M_\odot \text{ yr}^{-1}$ and a median value of $10^{1.48} M_\odot \text{ yr}^{-1}$. Our [OIII] emitters lie above the normal SFR- M_* relation and below the M_* -metallicity relation;

(7) The $F_{\text{NUV}}/F_{\text{FUV}}$ ratios of our [OIII] emitters are positively correlated with redshift, as a result of Lyman break absorption;

(8) Our [OIII] emitters exhibit remarkably high line luminosity – 18/22 have $L_{[\text{OIII}]\lambda 5007} > 5 \times 10^{42} \text{ erg s}^{-1}$ and 5/22 have $L_{[\text{OIII}]\lambda 5007} > 10^{43} \text{ erg s}^{-1}$;

(9) The estimated volume number density of [OIII] emitters at $z \sim 0.5$ is $\sim 3 \times 10^{-8} \text{ Mpc}^{-3}$, indicative of a steep slope at the bright end of the [OIII] LF.

We thank Chun Ly for constructive suggestions and helpful discussions. Z. L is grateful for support from UCLA-CSST Program for undergraduate research.

REFERENCES

- Atek, H. et al. 2014, ApJ, 789, 96, [ADS, 1406.4132](#)
— 2010, ApJ, 723, 104, [ADS, 1005.4068](#)
— 2011, ApJ, 743, 121, [ADS, 1109.0639](#)
Bruzual, G., & Charlot, S. 2003, MNRAS, 344, 1000, [ADS, astro-ph/0309134](#)
Calzetti, D., Armus, L., Bohlin, R. C., Kinney, A. L., Koornneef, J., & Storchi-Bergmann, T. 2000, ApJ, 533, 682, [ADS, astro-ph/9911459](#)
Cardamone, C. et al. 2009, MNRAS, 399, 1191, [ADS, 0907.4155](#)
Cardelli, J. A., Clayton, G. C., & Mathis, J. S. 1989, ApJ, 345, 245, [ADS](#)
Chabrier, G. 2003, PASP, 115, 763, [ADS, astro-ph/0304382](#)
Cutri, R. M. et al. 2013, Explanatory Supplement to the ALLWISE Data Release Products, Tech. rep., [ADS](#)
Draine, B. T., & Li, A. 2007, ApJ, 657, 810, [ADS, astro-ph/0608003](#)
Elbaz, D. et al. 2007, A&A, 468, 33, [ADS, astro-ph/0703653](#)
Izotov, Y. I., Guseva, N. G., Fricke, K. J., & Henkel, C. 2011, A&A, 536, L7, [ADS, 1111.5450](#)
— 2014, A&A, 561, A33, [ADS, 1310.1559](#)
Izotov, Y. I., Stasińska, G., Meynet, G., Guseva, N. G., & Thuan, T. X. 2006, A&A, 448, 955, [ADS, astro-ph/0511644](#)
Jarrett, T. H. et al. 2012, AJ, 144, 68, [ADS, 1208.0362](#)
Jaskot, A. E., & Oey, M. S. 2013, ApJ, 766, 91, [ADS, 1301.0530](#)
Kauffmann, G. et al. 2003, MNRAS, 346, 1055, [ADS, astro-ph/0304239](#)
Kewley, L. J., & Dopita, M. A. 2002, ApJS, 142, 35, [ADS, astro-ph/0206495](#)
Kewley, L. J., Groves, B., Kauffmann, G., & Heckman, T. 2006, MNRAS, 372, 961, [ADS, astro-ph/0605681](#)
Lilly, S. J., Carollo, C. M., & Stockton, A. N. 2003, ApJ, 597, 730, [ADS, astro-ph/0307300](#)
Ly, C., Malhotra, S., Malkan, M. A., Rigby, J. R., Kashikawa, N., de los Reyes, M. A., & Rhoads, J. E. 2016a, ApJS, 226, 5, [ADS, 1602.01089](#)
Ly, C. et al. 2007, ApJ, 657, 738, [ADS, astro-ph/0610846](#)
Ly, C., Malkan, M. A., Rigby, J. R., & Nagao, T. 2016b, ApJ, 828, 67, [ADS, 1602.01098](#)
Malkan, M. A., Jensen, L. D., Rodríguez, D. R., Spinoglio, L., & Rush, B. 2017, ArXiv e-prints, [ADS, 1708.08563](#)
Masters, D. et al. 2014, ApJ, 785, 153, [ADS, 1402.0510](#)
Nicholls, D. C., Dopita, M. A., Sutherland, R. S., Jerjen, H., & Kewley, L. J. 2014, ApJ, 790, 75, [ADS, 1405.7170](#)
Noeske, K. G. et al. 2007, ApJL, 660, L43, [ADS, astro-ph/0701924](#)
Noll, S., Burgarella, D., Giovannoli, E., Buat, V., Marcellac, D., & Muñoz-Mateos, J. C. 2009, A&A, 507, 1793, [ADS, 0909.5439](#)
Pâris, I. et al. 2017, A&A, 597, A79, [ADS, 1608.06483](#)
Peng, Y.-j. et al. 2010, ApJ, 721, 193, [ADS, 1003.4747](#)
Planck Collaboration et al. 2016, A&A, 594, A13, [ADS, 1502.01589](#)
Savaglio, S. et al. 2005, ApJ, 635, 260, [ADS, astro-ph/0508407](#)
Strom, A. L., Steidel, C. C., Rudie, G. C., Trainor, R. F., Pettini, M., & Reddy, N. A. 2017, ApJ, 836, 164, [ADS, 1608.02587](#)
Tremonti, C. A. et al. 2004, ApJ, 613, 898, [ADS, astro-ph/0405537](#)
Yang, H. et al. 2017a, ApJ, 844, 171, [ADS, 1701.01857](#)
Yang, H., Malhotra, S., Rhoads, J. E., & Wang, J. 2017b, ArXiv e-prints, [ADS, 1706.02819](#)

APPENDIX

A. BROADBAND PHOTOMETRIC SELECTION CRITERIA

We present our broadband photometric selection criteria in SQL query form here. To make our search as exhaustive as possible, we only use model magnitudes instead of other types of magnitudes. We also did not require clean photometry in the initial search. Our search derived a list of 2658 unique objects in total, which is available in a machine-readable format online.

```
SELECT ra, dec, field, mode, type, clean, probPSF, modelmag_u, modelmag_g,
modelmag_r, modelmag_i, modelmag_z into mydb.OIII FROM PhotoPrimary
WHERE modelmag_r>=18.5 and modelmag_z>=18.5
and modelmag_i-modelmag_z<=modelmag_r-modelmag_i-0.7
and modelmag_u-modelmag_g<=0.3 and modelmag_g-modelmag_r<=0.45 and
modelmag_r-modelmag_z<=0.8
and modelmagerr_u<0.25 and modelmagerr_g<0.15 modelmagerr_r<0.15 and
modelmagerr_i<0.15 and modelmagerr_z<0.15
and modelmagerr_u>0 and modelmagerr_g>0 and modelmagerr_r>0 and modelmagerr_i>0 and
modelmagerr_z>0
```

B. SEDS AND SDSS SPECTRA OF 22 [OIII] EMITTERS

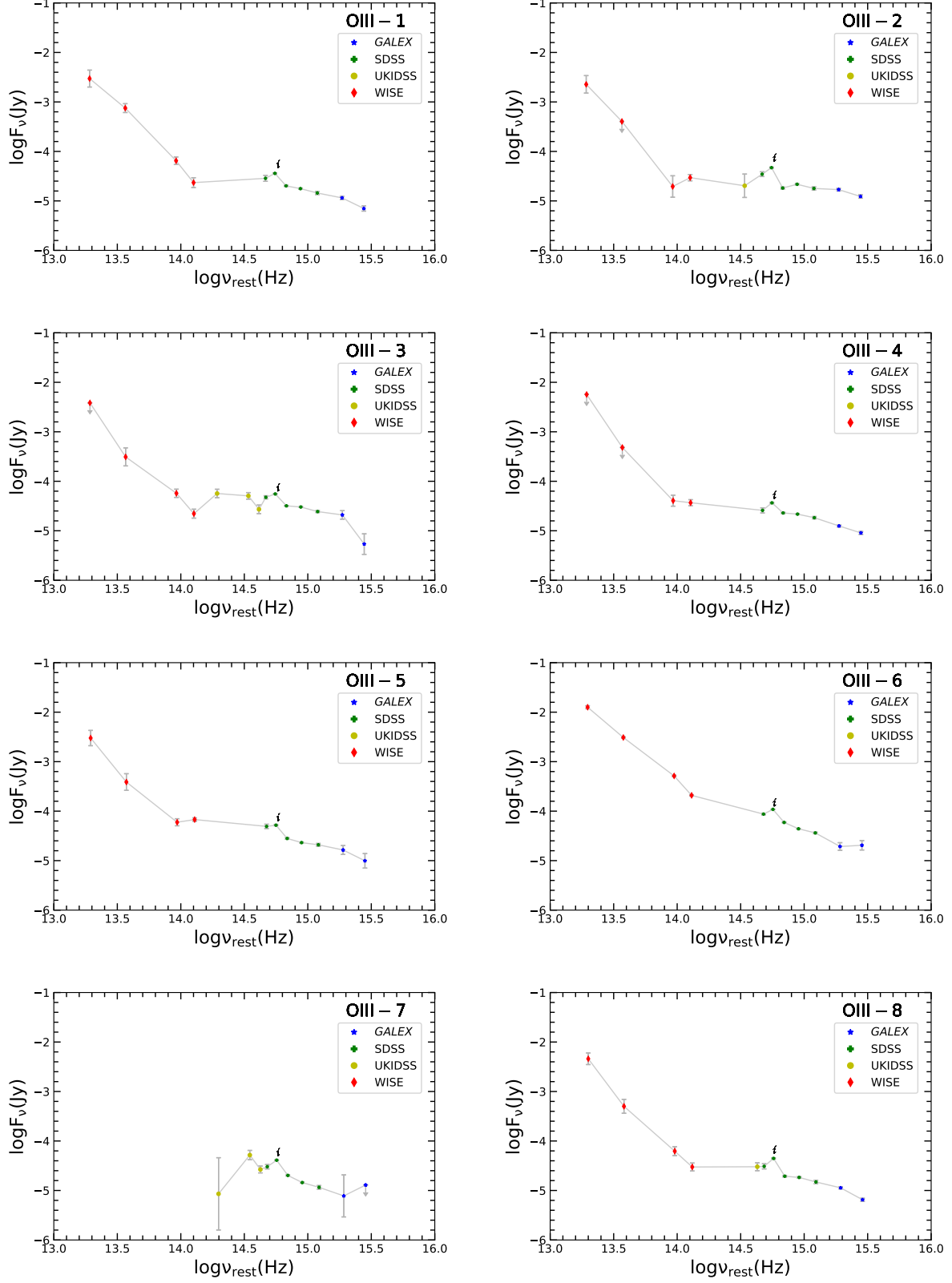


Figure B1. SEDs of 22 [OIII] emitters.

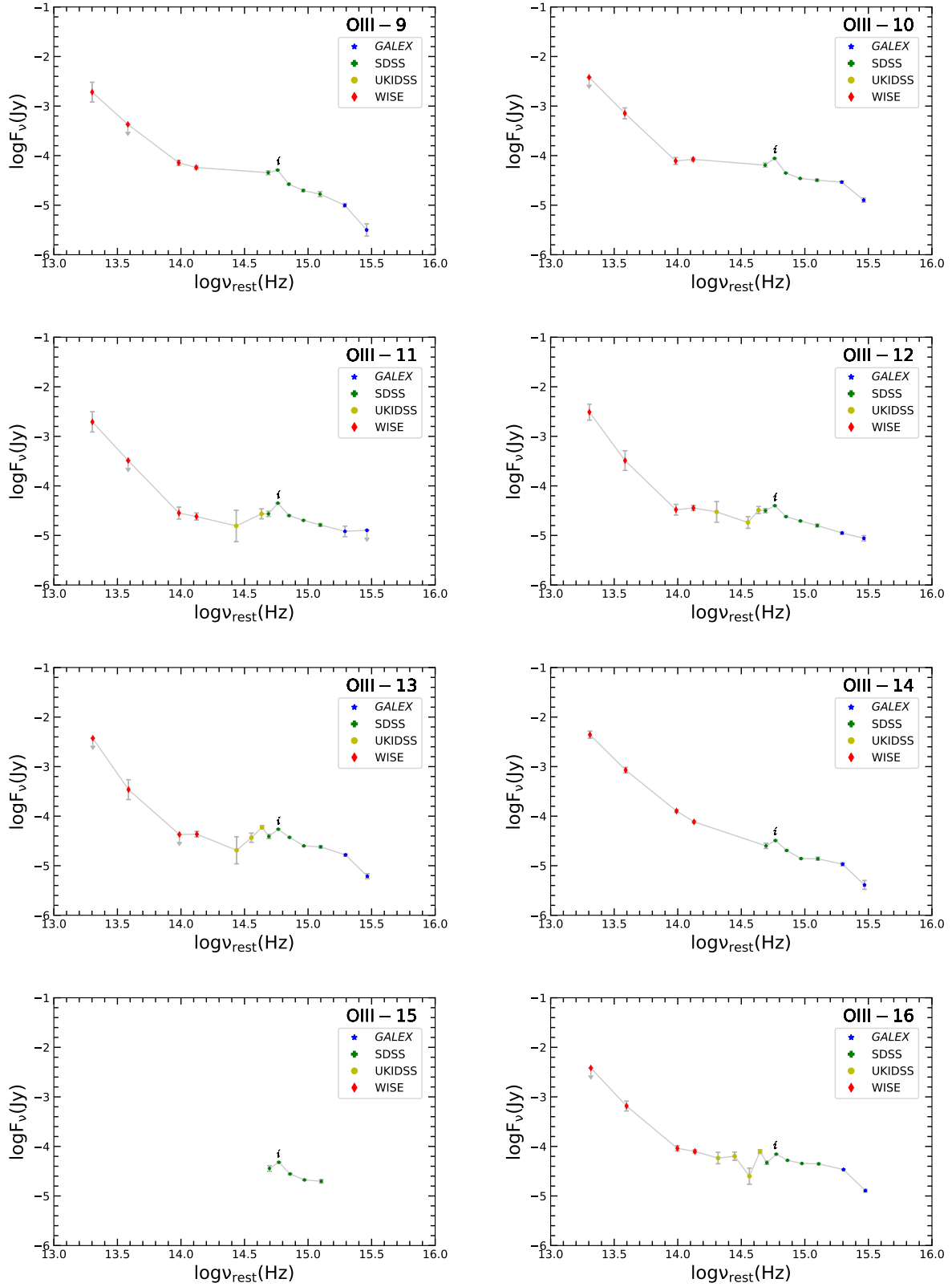


Figure B2. SEDs of 22 [OIII] emitters.

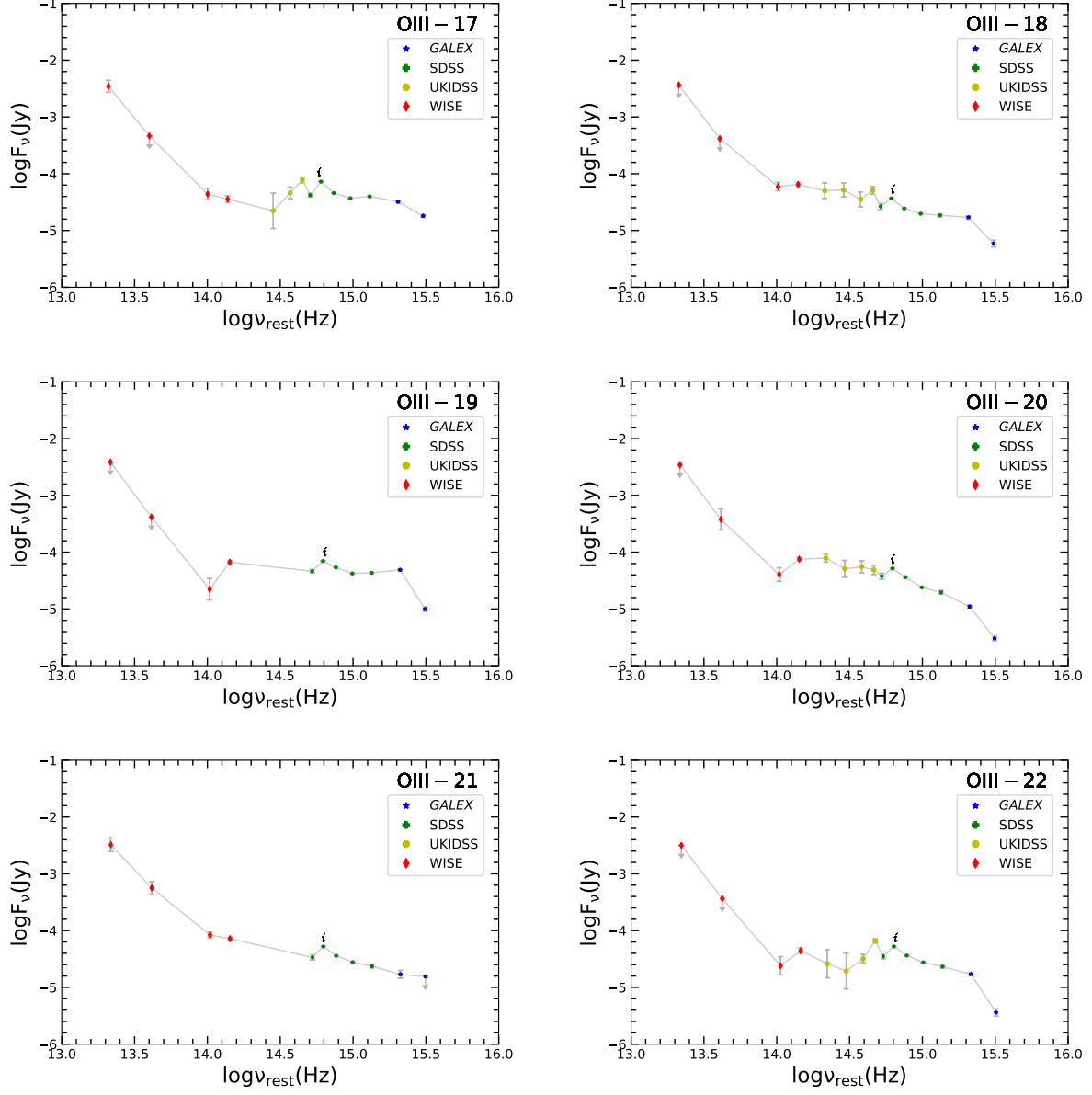


Figure B3. SEDs of 22 [OIII] emitters.

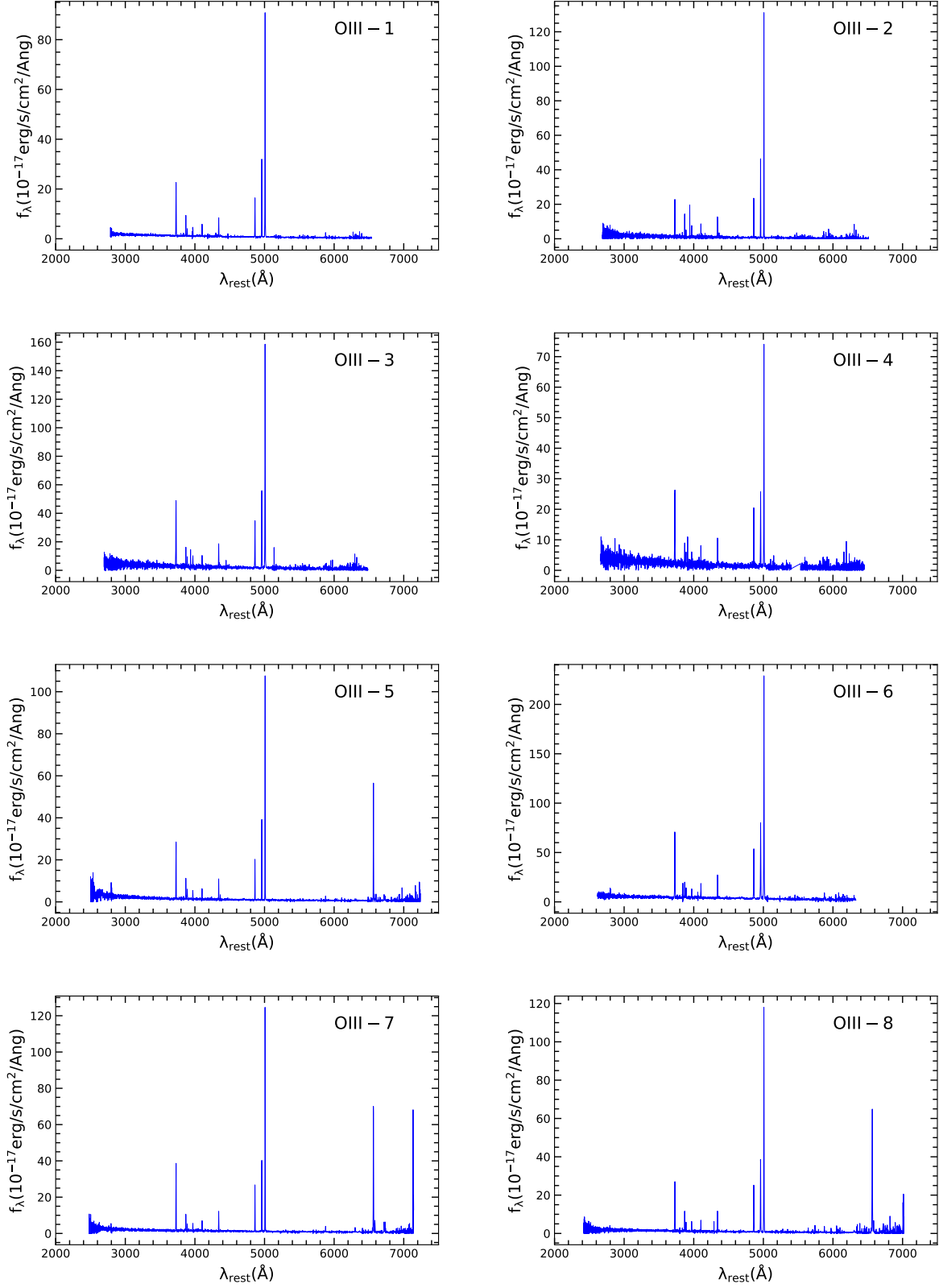


Figure B4. Rest-frame spectra of 22 [OIII] emitters. The spectra are taken from SDSS DR14.

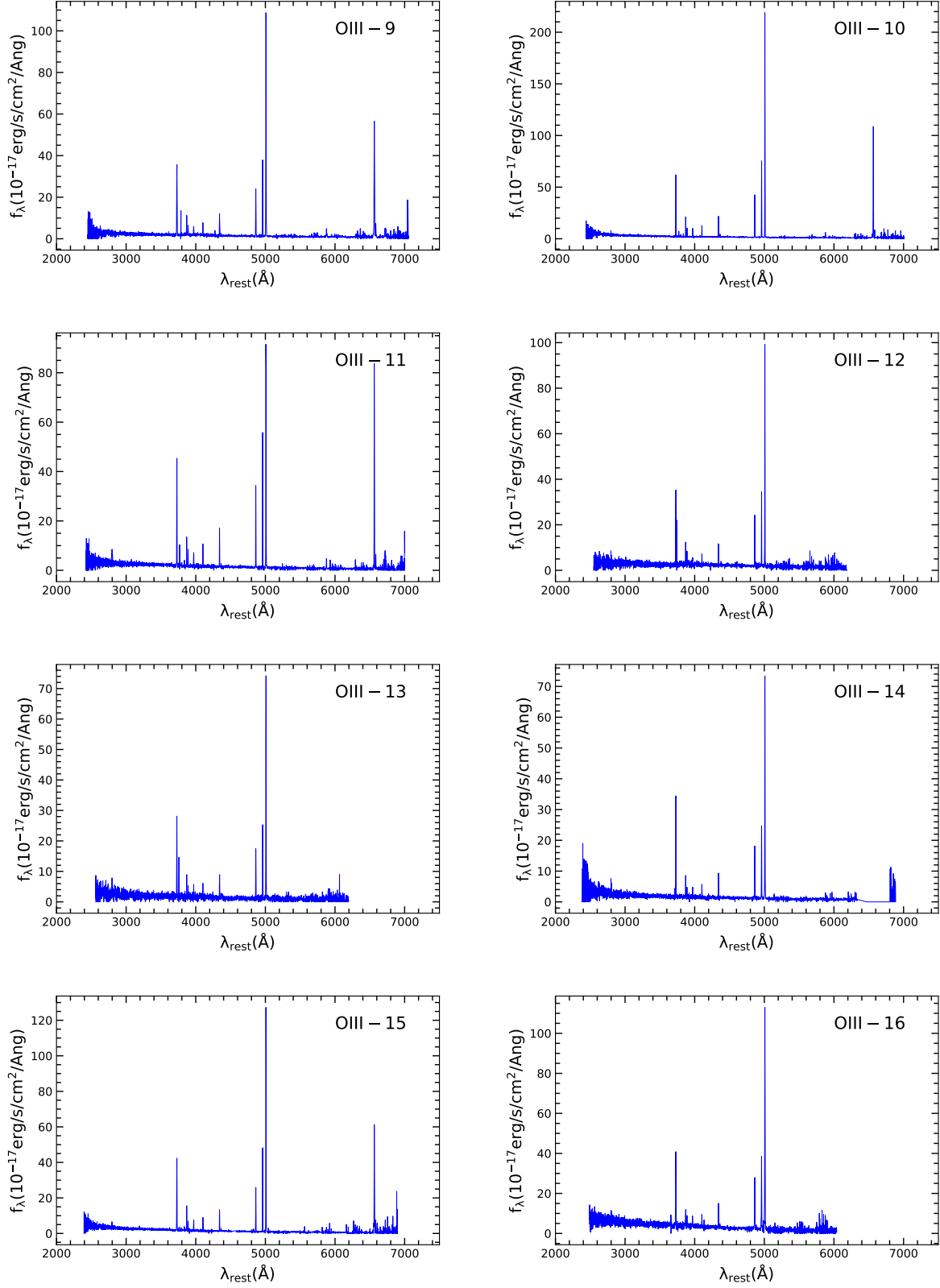


Figure B5. Rest-frame spectra of 22 [OIII] emitters. The spectra are taken from SDSS DR14.

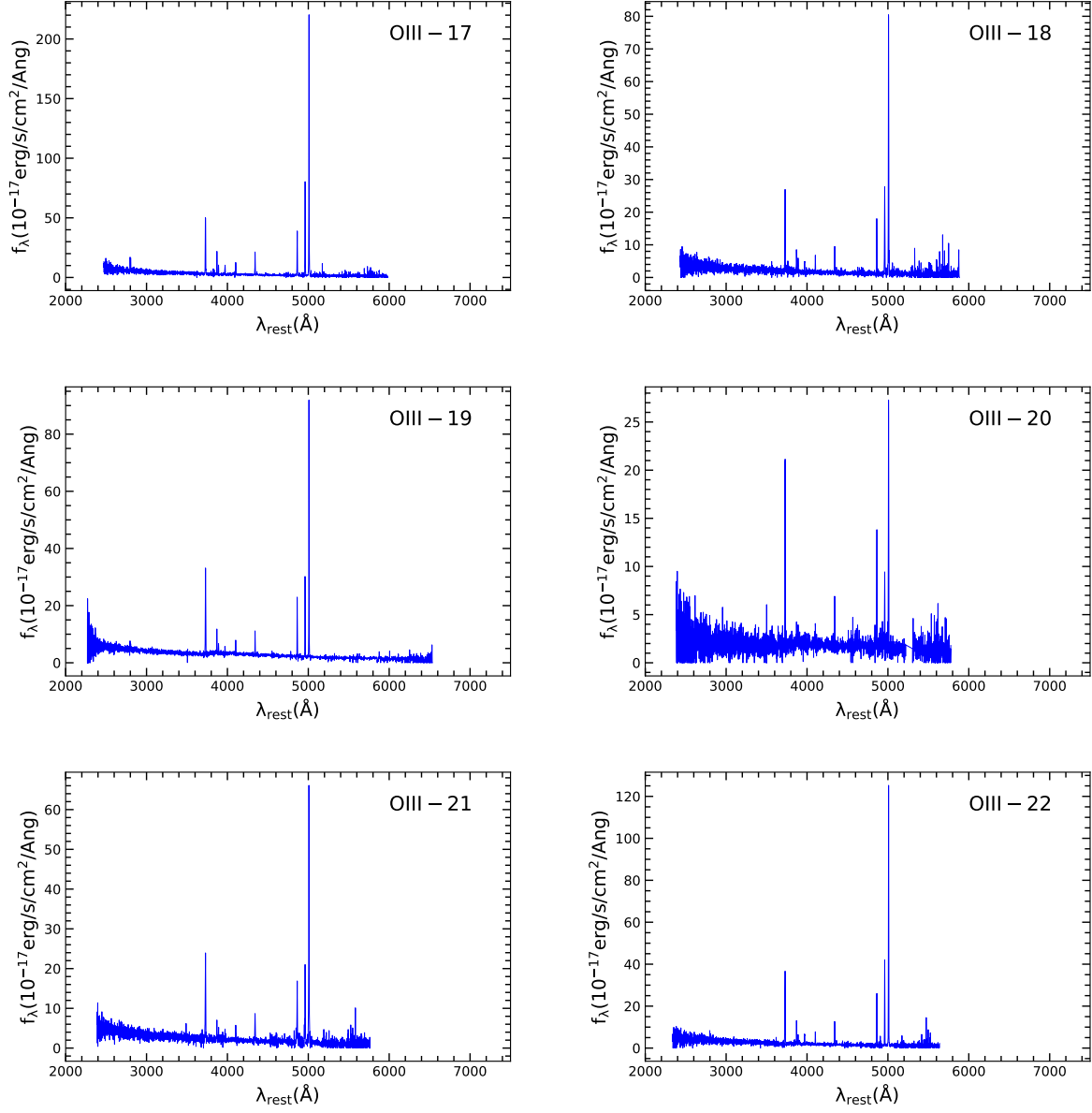


Figure B6. Rest-frame spectra of 22 [OIII] emitters. The spectra are taken from SDSS DR14.